Materials Today Chemistry 38 (2024) 102126

Contents lists available at ScienceDirect

Materials Today Chemistry

journal homepage: www.journals.elsevier.com/materials-today-chemistry/

Insight into titanium and zirconium phosphate-based materials for reactive surfaces

Claudio Imparato [a], Elisabetta Finocchio [b], Sebastiano Campisi [c], Michele Bigica [c], Antonella Gervasini [c,**], Aurelio Bifulco [a], Roberto Avolio [d], Nigel J. Clayden [e], Maria E. Errico [d], Antonio Aronne [a,*]

[a] Dipartimento di Ingegneria Chimica, dei Materiali e della Produzione Industriale, Università degli Studi di Napoli Federico II, P.le Tecchio 80, 80125, Naples, Italy
[b] Dipartimento di Ingegneria Civile, Chimica e Ambientale, Università degli Studi di Genova, Via Opera Pia 15, 16145, Genoa, Italy
[c] Dipartimento di Chimica, Università degli Studi di Milano, Via Camillo Golgi 19, 20133, Milan, Italy
[d] Institute for Polymers, Composites and Biomaterials, National Research Council of Italy, Via Campi Flegrei 34, 80078, Pozzuoli, Naples, Italy
[e] School of Chemistry, University of East Anglia, Norwich, NR4 7TJ, UK

ARTICLE INFO

Keywords:
Transition metal phosphate
Sol-gel synthesis
Sustainable production
Surface acidity
Solid acid catalyst

ABSTRACT

Transition metal phosphates are promising acid catalysts for biorefinery processes, and their efficiency can benefit from the dispersion in a porous support. Here, a one-pot hydrolytic sol-gel route is established for the synthesis of Ti–P–Si and Zr–P–Si oxides, comprising a fine distribution of titanium or zirconium oxophosphate in a silicate network. The environmental sustainability of the procedure, given by the choice of the starting materials and operating conditions, is attested by a comparative study of E factors. A deep structural and surface characterization, by solid state NMR, FTIR and XPS, reveals the evolution of the materials during thermal treatment and the presence of a diverse phosphorus unit connectivity, including P–O–Ti and P–O–Zr bonding that anchors P in the amorphous cross-linked silicate matrix. The materials are prevalently microporous, with specific surface areas around 400 $m^2\ g^{-1}$, and show a significant surface acidity (acid sites density >0.70 mmol g^{-1} from NH_3 titration), despite the low metal and P content. Brønsted and Lewis acidic sites coexist at the surface, the former being predominant thanks to the contribution of both P–OH groups and some silanols whose acidity is increased by nearby coordinatively unsaturated metal ions. A proof of the reactivity of these materials is obtained in the hydrolysis of sucrose, that was selected as test reaction. The proposed sol-gel route affords a tight mixing of metal and phosphorus into the silica matrix that promotes the synergy of the components, enhancing their activity, and represents an effective sustainable approach toward supported functional metal phosphates.

1. Introduction

Transition metal phosphates (MePs) are widely applied in heterogeneous catalysis, electrocatalysis, energy conversion and storage and purification technologies, due to their functional surfaces and peculiar properties. They possess significant acidity, adsorption capacity, ion exchange capacity, and good proton conductivity [1,2]. The specific surface acidic properties of these materials make them suitable catalysts for important reactions of both petrochemical industry [3] and biorefinery [4], including several biomass transformation processes [5–12]. Titanium and zirconium are especially promising for the design of tuneable and reactive phosphate-based acid solids. Particularly, the versatility of metal (oxo)phosphates as acid catalysts is due to the coexistence of both Brønsted acid sites, mainly represented by P–OH groups, with the possible contribution of Me–OH sites, and Lewis acid sites, consisting in metal ions either bound to phosphate groups or isolated, as in metal oxide phases [8,13].

Among the possible routes for the synthesis of metal (oxo)phosphate materials with crystalline or amorphous structure, wet chemical methods, like sol-gel, precipitation, evaporation-induced self-assembly and hydrothermal techniques, are chiefly employed. For example, zirconium and titanium phosphates were prepared starting from inorganic or alkoxide metal precursors in the presence of excess phosphoric acid [14] or phosphate salts [15]. Supporting metal-based species on a matrix

* Corresponding author.
** Corresponding author.
E-mail addresses: antonella.gervasini@unimi.it (A. Gervasini), antonio.aronne@unina.it (A. Aronne).

https://doi.org/10.1016/j.mtchem.2024.102126
Received 29 January 2024; Received in revised form 24 April 2024; Accepted 19 May 2024
Available online 23 May 2024

with large surface area and defined porosity, such as silica or aluminosilicates, is a convenient way to better exploit their catalytic properties [16,17]. The proper distribution of MeP units over a porous support can emphasize their acidity, adsorption capacity or proton conductivity, allowing the use of lower amounts of metal and P, as shown by the insertion of Ti and Zr in phosphosilicate glasses, which enhanced their performances and stability as proton exchange membranes in fuel cells [18,19]. This approach may also allow the modulation of surface acid sites and contrast phosphate leaching. Indeed, a limitation in the application of phosphate solids in water environment is their instability, because the high affinity of phosphorus to water promotes the hydrolysis of P–O–Me bonds and the consequent release of phosphate species in solution, especially at high temperatures [12]. With the aim to embed MePs in a versatile, stable and inexpensive support such as SiO_2, Ti–P–Si and Zr–P–Si ternary materials were usually prepared through grafting or impregnation in two- or three-step methods, using metal alkoxides and $POCl_3$ or H_3PO_4 as precursors [12,20–24]. An alternative approach is a one-pot sol-gel process, which enables the realization of a homogeneous dispersion of the active phase during the growth of the host material [19,25,26]. This was shown for the Nb–P–Si catalysts synthesized by a recently established sol-gel route [25,27] and tested in different reactions [28–31]. The introduction of transition metals showing different Lewis acidity (such as Ti or Zr) in a ternary oxide may deeply modify the distribution and strength of acid sites and thus the catalytic performances. However, preparing Ti–P–Si and Zr–P–Si ternary oxides by a single-step sol-gel procedure is a challenge because of the large difference in hydrolytic reactivity between the alkoxide precursors of these metals and tetraethoxysilane (the most common Si precursor). It becomes even more complicated when phosphoric acid is involved, due to its fast reaction rates. Indeed, while SiO_2–TiO_2 and SiO_2–ZrO_2 binary ceramics are well studied in the literature, only few works reported the sol-gel synthesis of such ternary systems, and they mainly focused on the proton conductivity properties [18,19], besides Paul et al., who prepared a Si–Ti phosphate (1:1:0.5 Si:Ti:P molar ratio) for catalytic purposes by using trimethyl phosphite, a copolymer template and HCl [32].

In this work, a new single-step hydrolytic sol-gel procedure, inspired by several principles of green chemistry, such as waste prevention, energy efficiency, less hazardous chemical synthesis, and the use of safer solvents, was established to obtain Ti–P–Si and Zr–P–Si mixed oxide gels. To mitigate the depletion of critical raw materials and natural resources, low contents of both Me and P were employed. Moreover, phosphoric acid was chosen as inexpensive and green P precursor and no additional mineral acids and templating agents were used. The environmental (E) factors were determined as representative green metrics to quantify the amount of waste produced in the synthetic process, highlighting the sustainability and advantages of the proposed route compared to existing ones. The acidity of the prepared materials has been successfully studied by the adsorption of a strong base, such as pyridine, that can detect simultaneously and unambiguously both Brønsted and Lewis sites exposed over complex surfaces [33,34]. Also, the effective acidity of the samples was verified in the sucrose hydrolysis reaction, chosen as test reaction. The thorough structural and surface characterization shows the relationship between the composition, network cross-linking, acid sites distribution and catalytic performances of these ternary oxides.

2. Experimental

2.1. Synthesis of the materials

In the synthesis of Me–P–Si oxides (Me = Ti or Zr), tetraethoxysilane, $Si(OC_2H_5)_4$ (*TEOS*, 98 %), zirconium(IV) propoxide, $Zr(OC_3H_7)_4$ (70 wt % in 1-propanol), titanium(IV) n-butoxide, $Ti(OC_4H_9)_4$ (>97 %) and orthophosphoric acid, H_3PO_4 (85 wt% aqueous solution) were chosen as precursors. Acetylacetone (*Hacac*, >99 %), acetic acid (*AcOH*, 99 %) and ethanol (*EtOH*, >99.8 %) were employed as stabilizing agent, catalyst and solvent, respectively. All chemicals were provided by Sigma-Aldrich and used without further purification.

The ternary oxides were synthesized by a hydrolytic sol-gel route, developed and optimized by changing the process variables (including concentration of the reagents and mixing order) with the aim of obtaining homogeneous chemical gels. In a typical procedure, carried out at room temperature, two solutions were prepared: one containing *TEOS*, *EtOH* and H_3PO_4 (solution A), and the other containing the metal alkoxide, *EtOH* and *Hacac* (solution B). The former was magnetically stirred for 30 min, the latter for 15 min. Then solution A was added to solution B, and after stirring the mixture for 30 min, a suitable volume of acetic acid was added to lower the pH in the range 4–5. After 30 min, the addition of water (with *EtOH* in 1:1 v/v ratio) started, split in five portions added within 24 h. The gelation occurred in about 6 days in optimal conditions, producing a yellow-coloured homogeneous gel (see Figure S1). The wet gel was aged for 2 days, then dried in a ventilated oven at a temperature rising from 80 to 100 °C. Finally, the xerogel was ground and calcined in a tubular furnace under airflow at 500 °C for 1 h, with a heating rate of 10 °C/min. The flow-chart of the synthetic procedure is shown in Scheme 1 and the molar ratios between the reagents, additives and solvent are reported in Table S1.

Two mixed oxide samples were prepared, with nominal molar composition 10 TiO_2 • 2.5 P_2O_5 • 87.5 SiO_2 (**TiPSi**) and 10 ZrO_2 • 2.5 P_2O_5 • 87.5 SiO_2 (**ZrPSi**), both having a Me/P atom ratio equal to 2 (see Table S2). The xerogels characterized before the calcination are indicated as TiPSi-gel and ZrPSi-gel. A P_2O_5–SiO_2 (PSi) sample was synthesized as reference for IR spectroscopy studies, starting from TEOS and H_3PO_4, following the same drying and calcination procedure of the ternary gels.

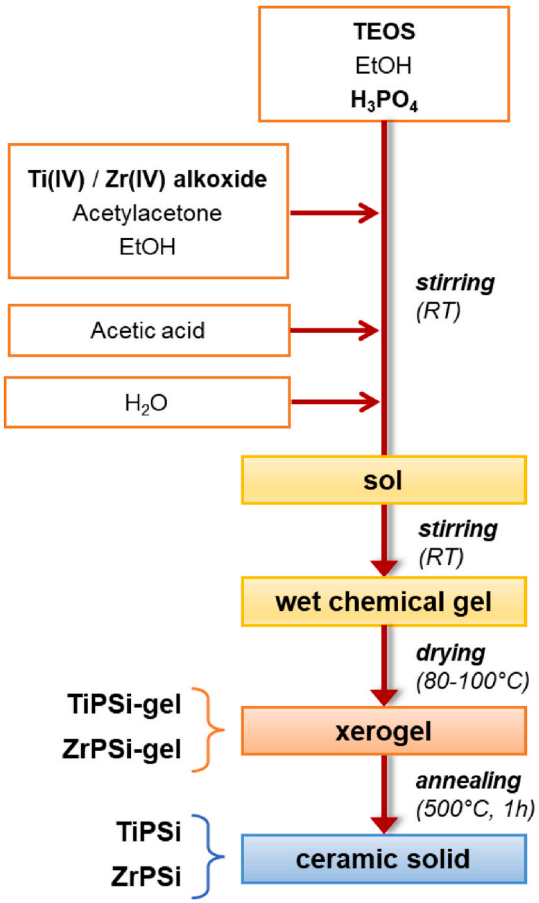

Scheme 1. Flow-chart of the sol-gel synthesis procedure of TiPSi and ZrPSi ternary oxides.

2.2. Characterization

Thermogravimetric-differential thermal analysis (TG-DTA) was performed by a SDT Q600 simultaneous thermoanalyser (TA Instruments), heating in nitrogen at 10 °C/min rate.

X-ray diffraction (XRD) measurements were performed on a Philips X'PERT-PRO diffractometer with monochromatized CuKα radiation (40 mA, 40 kV) at a step width of 0.013° (2θ).

Skeletal spectra of catalyst powders diluted in KBr have been recorded in a Nicolet 5700 FTIR instrument (Thermo Fisher), collecting 64 scans with a resolution of 2 cm^{-1} and background air. Pyridine adsorption and desorption experiments have been carried out over pure powder disks (20 mg average disks) in a conventional gas manipulation apparatus. Before any adsorption experiment, samples have been activated in vacuum (10^{-3} torr) for 1 h at 480 °C. Pyridine adsorption was performed at room temperature and following outgassing at increasing temperatures in the range 150–350 °C. Spectra of the surface species were recorded at each adsorption/desorption step, using a Thermonicolet Nexus instrument (4 cm^{-1} resolution, 100 scans, OMNIC software). The reported subtraction spectra are obtained by subtracting the spectrum of the activated catalyst surface (i.e. after outgassing at high temperature) from the spectrum of the catalyst after pyridine vapor adsorption.

Solid-state ^{29}Si and ^{31}P NMR spectra were collected on a Bruker Avance II 400 spectrometer (Bruker Biospin, Milan, Italy) operating at a static field of 9.4 T and equipped with a 4 mm broadband magic angle spinning (MAS) probe. Powder samples were packed in 4 mm zirconia rotors sealed with Kel-F caps. A direct polarization (DP) scheme with high power proton decoupling was applied with the following parameters: for ^{29}Si, a π/2 pulse width of 5 μs, a recycle delay of 200 s and 2048 scans; for ^{31}P, a π/2 pulse width of 4.9 μs, a recycle delay of 180 s and 512 scans. ^{29}Si and ^{31}P experiments were performed at 6 and 9 kHz spinning rate, respectively.

X-ray Photoelectron Spectroscopy (XPS) analyses were performed on an M-PROBE Surface Spectrometer with an Al (Kα) source and a spot size from 0.15 mm to 1 mm in diameter. A 10 V applied voltage at a vacuum of 10^{-7} –10^{-8} Torr was used. The survey scans were investigated in 0–1100 eV binding energy range, using a spot size of 800 μm with an energy resolution of 4 eV (scan rate of 1 eV per step). ESCA Hawk Software was used for data curation. All the resulting binding energy values were corrected using the C 1s peak (C–C) fixed at 285 eV as a reference. Interval of binding energies for Si 2p, P 2p, O 1s, Ti 2p and Zr 3d were 102.3–102.9 eV, 133.7–133.9 eV, 532.0–532.5 eV, 459.2–459.5 eV, and 183.2–183.3 eV, respectively.

The determination of specific surface area (SSA) and porosity of samples was performed by physical adsorption/desorption isotherms of inert gas (N_2, 99.9995 % purity) at −196 °C. Isotherms were collected in a Sorptomatic 1900 (Carlo Erba Instrument) working with static method. Prior to the analysis, the samples were pressed, crushed, and sieved to obtain particles in the range of 80–200 mesh. Then, the samples (about 0.2 g) were outgassed at 150 °C for 16 h under vacuum (10^{-2} torr) to remove water and other volatile organic compounds adsorbed on the surface. The specific surface areas were calculated by using 3-parameter BET (Brunauer-Emmet-Teller) equation in the pressure range $0.005 < p/p_0 < 0.4$. Micropore size distribution analysis was performed by applying the Horvath-Kawazoe (HK) model equation to the corresponding adsorption branch of N_2 isotherm (in the pressure range $0 < p/p_0 < 0.35$).

Acid site number was determined by gas-solid titrations by NH_3 probe adsorption in flowing dynamic experiments [35]. Measurements were carried out in a home-made adsorption line equipped with mass flow controllers, an electrical vertical oven for temperature control and an online FT-IR spectrophotometer (Bio-Rad with DTGS detector). A quartz reactor packed with sample particles (*ca.* 0.06 g, 45–60 mesh) was placed inside the oven. The samples were pre-treated at 350 °C under flowing air (0.5 L h^{-1}) for 4 h prior to the measurements to desorb impurities and remove physically adsorbed water. After cooling down to 80 °C, a NH_3/N_2 mixture, with NH_3 concentration of *ca.* 5000 ppm flowed at 2 NL h^{-1} through the reactor maintained a constant temperature (T = 80 °C). The gas flow at the outlet of the reactor entered into a gas cell (path length 2.4 m multiple reflection gas cell) in the beam of the FT-IR spectrophotometer where it was measured online (monitoring NH_3 line at 966 cm^{-1}, N–H asymmetric stretching, wagging mode). The number of acid sites (in μequiv·g^{-1}) was determined by quantitatively evaluating the adsorbed NH_3.

2.3. Catalytic model reaction

Sucrose hydrolysis was used as a test reaction to characterize the surface reactivity of calcined samples [36]. The tests have been carried out dispersing 0.3 g of each sample in 150 mL of 50 mM aqueous sucrose solution in a glass slurry batch reactor (Syrris, Atlas, Royston, UK) with magnetic stirrer at a constant rate of 800 rpm under increasing temperature from 50 to 90 °C (0.12 °C min^{-1}). At the end of the temperature ramp, the reaction proceeded under isothermal conditions at 90 °C for 16 h. The sucrose and formed products were quantified in a high-performance liquid chromatograph (HPLC) with a refractive index detector (Waters 410). A Sugar-Pack (I300 × 6.5 mm, 10 μm particle size, Waters) column operating at 90 °C and eluted with an aqueous solution of Ca–EDTA (10^{-4} M) was used.

Sucrose conversion was computed according to the following equation:

$$conversion\ \% = 100 \bullet \frac{[sucrose]_o - [sucrose]_t}{[sucrose]_o} \quad (1)$$

For the identification and quantification of the products, calibration lines for HPLC were used. The area of each possible product was used to calculate the number of moles, the carbon balance, the conversion and the selectivity towards each sugar.

For the determination of activation parameters, the same approach as that presented in Ref. [37] was followed. The kinetic coefficients (k_{Tm}) were computed at the average temperature T_m between two samplings according to the following equation:

$$k_{Tm} = (\Delta C / \Delta t)/C_m \quad (2)$$

where Δt is the time interval between two samplings (Δt = 0.5 h and ΔT = 5 °C); ΔC is the variation of sucrose concentration between two samplings; C_m is the average sucrose concentration between two samplings.

The values of activation energy and pre-exponential factor were then evaluated by the classical Arrhenius approach by reporting ln (k_{Tm}) vs. $1/T_m$. The obtained plots and activation parameters are reported in Figure S2 and Table S3, respectively, of the Supplementary material.

3. Results and discussion

3.1. Sol-gel synthesis of the ternary oxides

The composition of the Me–P–Si oxides was chosen on the basis of previous studies on the Nb–P–Si system, which revealed a higher density and strength of acid sites with lower Nb and P content, as a consequence of the larger surface area and better active site distribution [29], and indicated an increase of phosphate stability by doubling the Nb/P molar ratio (from 1 to 2) [30]. The hydrolytic sol-gel synthesis of TiPSi and ZrPSi chemical gels required a new procedure to be set up because of the different properties and reactivity of the metal precursors. Matching the reaction rates of all the precursors is vital to produce uniform networks. Indeed, a first difficulty in the cross-condensation of silicon with titanium or zirconium starting from alkoxides is the large difference in reactivity of these precursors in the nucleophilic substitutions, which easily causes phase separation after the addition of water. The

hydrolysis rates of Ti and Zr alkoxides are much faster than that of *TEOS*, because of the lower electronegativity of the metal atoms compared to Si and their ability to expand their coordination sphere. Therefore, a pre-hydrolysis of *TEOS* in acidic aqueous solution is often performed, accompanied by the addition of a complexing agent for the metal [38]. Here another challenge is the use of H_3PO_4 as P precursor, since hydrogen phosphate species ($H_{3-x}PO_4^{x-}$) have high complexing ability and affinity for the metals [39]. This was confirmed by the appearance of precipitates when H_3PO_4 was added to the metal alkoxide solution, likely due to the rapid formation of insoluble metal oxophosphate species. Moreover, the high Si/Me ratio means that very large H_2O/Me ratios are reached, making the control of hydrolysis rates more difficult.

In our work, these hurdles were overcome by carefully adjusting the process conditions, namely the composition of the reaction mixture and the order and timing of addition of the reagents. To avoid the contact of H_3PO_4 with the metal complexes in a concentrated solution, it was added to the *TEOS* solution instead. At this stage, *TEOS* hydrolysis can slowly start by effect of the small amount of water contained in 85 wt% H_3PO_4, and an initial cross-condensation cannot be excluded [40], although Si–O–P bonds are rather unstable in water [41] and in the mixed solution Si–O–Me–O–P bridging is expected to be favoured. To modulate the reactivity of Ti and Zr alkoxides, we chose acetylacetone, a commonly used β-diketone that forms strong bidentate coordination bonds with the Me cations, allowing control of the growth rate of oxo-alkoxide aggregates and in turn of the whole process [42]. Acetic acid was preferred to stronger and more hazardous mineral acids to lower the solution pH, also because acetate can coordinate Me ions, contributing to their stabilization [43]. It can be noted that different ratios of acetylacetone and acetic acid were needed to optimally stabilize the Ti and Zr species in the reaction mixture (see Table S1), without using other additives or structure-directing agents. The addition of water is the most delicate step in the sol-gel synthesis of a complex system. Since pouring the whole water volume into the solution resulted in turbidity of the mixture or partial gelation, the addition of the hydro-alcoholic solution was split in five successive steps, allowing gradual hydrolysis and condensation and finally providing chemical gels with a visual homogeneity (see Figure S1). Their yellow coloration was due to the formation of Ti- and Zr-acetylacetonate complexes whose charge transfer character induces an absorption band in the visible light range [44,45]. After calcination, white powders were produced.

3.2. Sustainability of the synthetic route

The proposed sol-gel procedure has several advantages from the viewpoint of sustainability. The obtainment of chemical gels in a one-pot process ensures that the precursors are almost completely incorporated into the final product, thus leading to high yields, minimized sub-products, and very low amounts of wasted reagents. In contrast to the production of nanoparticles, no centrifugation nor washing with solvents (i.e., side processes) is needed for the recovery and purification of the material. To compare the proposed synthetic strategy to existing technologies, a patent search for the production of similar materials was carried out. However, the most relevant patents deal with the preparation of titanium-containing silico-alumino-phosphates, with widely variable precursors and processing conditions (WO2012085150A2) or partially substituted aluminosilicate zeolitic materials (e.g., US10850265B2, CN103100415B), therefore these were not considered. In view of the above, Ti–P–Si was chosen as model material since more literature reports about this system. The procedures found in the scientific literature for the wet chemical synthesis of Ti–P–Si mixed oxides were summarized in Table S4, including the relative starting materials, their amounts, the operating conditions and the number of preparation steps. As regards the precursors, TEOS is almost invariably used for providing the silicate matrix, with the exception of the in situ preparation of sodium silicate from silica and NaOH [24], and the most common Ti(IV) alkoxides (n-butoxide or isopropoxide) are chosen for titanium. In the case of phosphorus, besides phosphoric acid, phosphoryl chloride, trimethyl phosphate and trimethyl phosphite have been used. $POCl_3$ is a toxic compound, having much lower LD_{50} and LC_{50} (inhalation) values than those available for the other P precursors [46], moreover it reacts quickly with water releasing an undesirable by-product as HCl. Trimethyl phosphate is a suspected carcinogen, whereas trimethyl phosphite is flammable and has higher acute toxicity than H_3PO_4. This latter may be therefore considered the least hazardous among these P sources. Most of the multistep procedures included large volumes of toluene for the impregnation steps, and all the analysed reports, except one [24], employed HCl or HNO_3 to adjust the pH. In our route, we used only ethanol as the solvent and avoided strong acids, opting for acetic acid as a safer alternative.

Various green metrics are available to quantitatively evaluate the sustainability of a chemical synthesis process. Atom economy is a direct indicator of the amount of reagent mass converted into the product. However, the variability in the products composition, the lack of information on the synthesis yields along with the use of solvents, auxiliaries and excess reagent in the impregnation step of some protocols make the atom economy hardly significative in the present case of study. Therefore, we focused on the environmental (E) factor, which takes into account the amount of waste produced in the process and is equal to the mass of waste generated per mass of product [47]. This means that the lower the E factor, the greener the process. The E factor is seen as a valuable metric to assess the fabrication of nanostructured materials [48], although it has been less frequently used in this scope than in organic synthesis, where it is increasingly employed to guide the design of the synthesis route. For example, E factors between 2.0 and 45.3 were calculated for different ordered mesoporous silicas [49], while an E factor about 15 was reported for the synthesis of dendritic silica nanoparticles by hydrolysis and condensation [50]. It is worth mentioning that a recent effort toward the intensification of manufacturing processes led to the production of alumina by coupling sol-gel chemistry with reactive extrusion, achieving an E factor of 3.4 [51].

We performed a comparison with four synthesis protocols of Ti–P–Si oxides, selecting the materials addressed to catalytic applications and taking as reference the sample closest to ours for the works that included different compositions. Details about the evaluation are reported in the Supplementary material (Section S3) and the retrieved data and results are listed in Table S5. To get a comprehensive view, we calculated the general E factor (EF), including all used substances except water, the simple E Factor (sEF), excluding water and solvents, and the complete E Factor (cEF), including all the used substances, assuming no recycling [47]. Only the latter two factors are shown in Fig. 1, for clarity. The

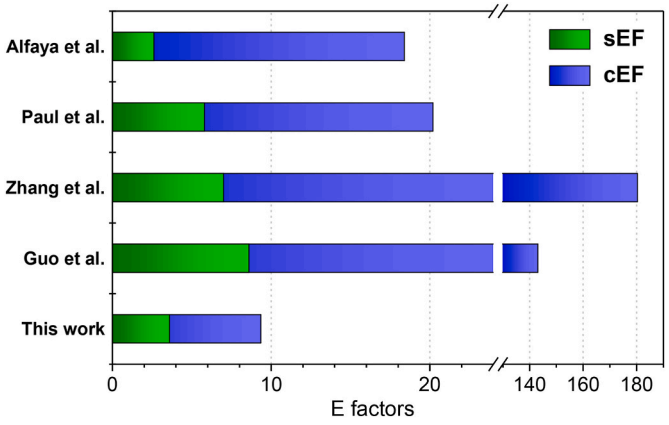

Fig. 1. Simple E Factor (sEF, green bars) and complete E Factor (cEF, blue bars) values for the synthesis of Ti–P–Si mixed oxides in selected literature works [12,20,22,32] and through the procedure adopted here. Details about the calculations are reported in section S2. (For interpretation of the references to colour in this figure legend, the reader is referred to the Web version of this article.)

synthesis of TiPSi described in this work is associated to a cEF of 9.4, an EF of 8.3 and a sEF of 3.6. For the synthesis of ZrPSi, the values are even lower (cEF = 7.5, EF = 6.6, sEF = 2.9). Interestingly, as can be observed in Fig. 1, all the evaluated reports result in higher cEF than our procedure. Only the procedure of Alfaya et al. [22] has a slightly lower sEF, since they used nitric acid without any other additives or auxiliaries. In the other works, the poloxamers (P123, F127) introduced as templates to obtain larger pore size and volume contributed to the increase of sEF. It can be noted that two- or three-step protocols inevitably raise the cEF due to the repeated impregnation and washing cycles, affecting also the sEF in case of abundant excess of reagents. However, even compared with the reference single-step protocol (Paul et al. [32]), we manage to significantly reduce the consumption of chemicals, which is highly desirable in the perspective of reducing the depletion of natural resources and endangered elements, such as phosphorus and titanium, featured in the 2023 EU list of critical raw materials.

Still, concerning the energy consumption, the thermal treatment is the most impactful stage. We perform a shorter isothermal heating of 1 h (at 500 °C) compared to other works (i.e., 6 h at 400 [32] or 550 °C [12] and even 5 days at 500 °C [22]) and do not need hydrothermal conditions (differently than Guo et al. [12] and Kovalchuk et al. [24]), which is favourable also in view of the scalability and industrialization of the process. Finally, the rather long gelation time is a factor that can be still optimized, for example by means of a mild heating that would accelerate the kinetics.

3.3. Structural characterization

Thermal analysis was performed on the dried gels to examine their thermal behaviour and determine the appropriate calcination temperature. The TGA and DTA curves recorded in nitrogen are shown in Figure S3. The overall mass loss, being 29 wt% for TiPSi-gel and 26 wt% for ZrPSi-gel, can be seen as the sum of three main steps, associated to endothermic DTA peaks. The first mass loss (of about 12 wt%), up to about 160 °C, is due to the vaporization of adsorbed water and residual alcohol molecules. The second mass loss, which takes place over a wide temperature range, and whose maximum rate is reached at about 238 °C for ZrPSi-gel and 312 °C for TiPSi-gel, is related to the volatilization or decomposition of acetate and acetylacetonate (*acac*) groups chemically bound to metal ions. Between 300 and 500 °C dehydroxylation steps also occur, as shown for titanium phosphates [52]. The remaining products derived from incomplete pyrolysis of the organics are almost completely removed above 550 °C, therefore an isothermal treatment in air for 1 h at 500 °C was carried out in the preparation of the final ternary oxides.

The structure of the dried and calcined gels was analysed by XRD, solid state NMR and FTIR spectroscopy. The XRD patterns (Figure S4) show the amorphous nature of all the materials, which attests that solid solutions were obtained, without any evident segregation of metal oxide, metal phosphate or other crystalline phases. The ^{29}Si and ^{31}P MAS NMR spectra of dried and heat-treated gels are displayed in Figs. 2 and 3, respectively. The Q_N notation was adopted to designate the extent of cross linking of silicon atoms, where Q_N indicates $Si(OSi)_N(OX)_{4-N}$ (X = P, H, Ti or Zr). For phosphorus atoms the analogous Q'_N notation stands for $OP(OP)_N(OX)_{3-N}$ (X = Si, H, Ti or Zr). Alternatively, the Q^n_m notation, where *n* and *m* represent the number of P–O–P and P–O–Me linkages, respectively [53], can be more informative in our case.

The various structural units are evaluated by curve fitting analysis of spectra using Gaussian functions. It is found that Q_N units occur in distinct chemical shift ranges (9–10 ppm intervals) allowing the fine determination of specific silicon coordination, while for ^{31}P NMR spectra broad resonances are observed preventing the resolution of individual resonances corresponding to all the different types of phosphorus coordination. Results of the curve fitting are displayed in Table 1. Both dried samples, regardless of the metal, have similar ^{29}Si NMR

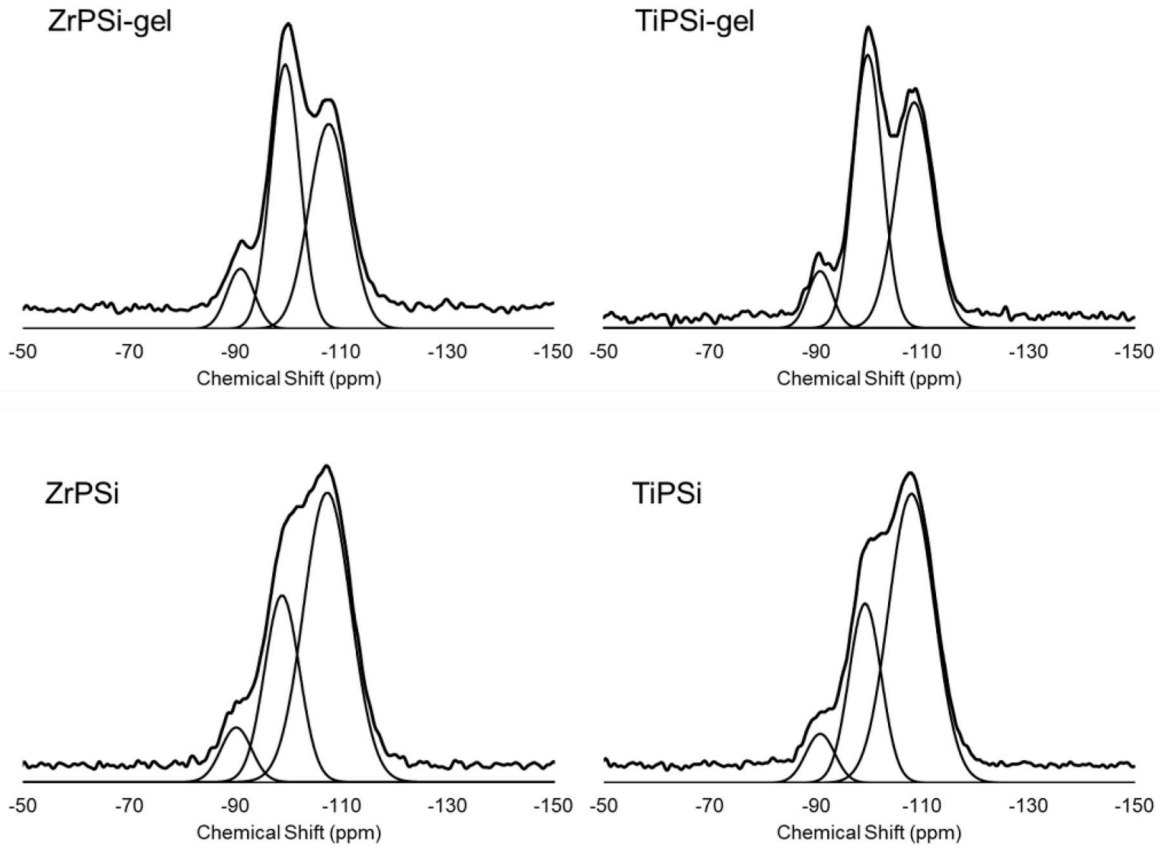

Fig. 2. ^{29}Si CP solid state NMR spectra recorded on ZrPSi and TiPSi dried gels and calcined samples. The results of line fitting are reported in Table 1.

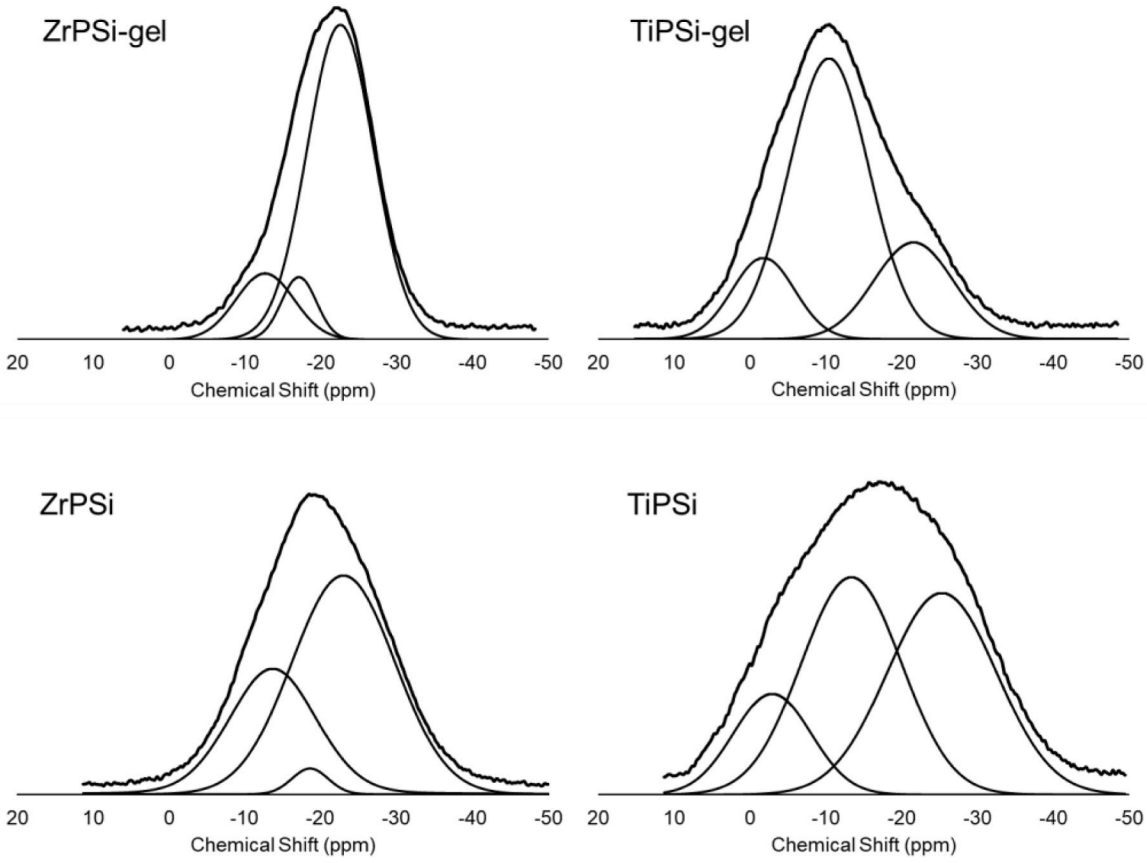

Fig. 3. ^{31}P DP solid state NMR spectra recorded on ZrPSi and TiPSi dried gels and calcined samples. The results of line fitting are reported in Table 1.

spectra with three resonances, at ca. −90, −99, and −107 ppm, assigned to Q_2, Q_3, and Q_4 structural units, respectively [54]. The predominance of Q_3 and Q_4 units (Table 1) indicates that the adopted synthesis conditions allowed the formation of highly cross-linked silicon-oxygen networks. The heat treatment at 500 °C leads to a small increase in the extent of the cross-linking through the condensation of Q_3 units leaving the amount of Q_2 unchanged. The analysis of the ^{29}Si spectra does not give any direct evidence for the manner in which the phosphorus and the metals (Ti or Zr) are incorporated into the silicon-oxygen matrix, even if the predominance of Q_3 units, whose relative intensity is about the same of that of Q_4 units in both dried gels, can be considered a clue for the existence of Si–O–Me bridges [55,56].

The curve fitting of ^{31}P NMR spectrum of TiPSi dried gel reveals the presence of a Q'_0 resonance, with a chemical shift around −1.8 ppm, probably related to uncondensed phosphate units trapped within the pore structure of the silicate framework, together with more shielded signals at ca. −10 and −22 ppm that are related to more polymerized units. On the contrary, in the deconvolution of ^{31}P NMR resonances of ZrPSi dried gel, the Q'_0 resonance does not appear, while signals at ca. −12 and −22 ppm are observed together with a less intense signal at −17 ppm.

In phosphosilicate networks, Q'_1, Q'_2 and Q'_3 sites are found in the ranges from −11 to −12 ppm, from −22 to −23 ppm and around −30 ppm, respectively [57]. Therefore, the main resonances observed in TiPSi and ZrPSi gels could be considered as signals of Q'_2 and Q'_3 ^{31}P species with a strong deshielding induced by the presence of a Me^{4+} ion coordination. However, metal phosphate structures (e.g., -P(OMe)$_2$ and -P(OMe)$_3$ connectivity) are likely prevalent, given the reactivity of the metal ions with phosphate [21,27,58] and the Me/P ratio. In a study about P species in aluminosilicate frameworks, signals in this range were attributed to a variety of units, mainly Q^1_1, i.e., simultaneously linked to a P and a metal atom [53]. Moreover, the possibility of bidentate coordination, also involving the P═O bond, which can lead to phosphate groups bonded by four bridging oxygens [52,53], and the intervention of Si might also be considered, making the picture rather complex.

Consequently, the structure of TiPSi-gel can be described as formed by a Si–O–Ti–O–P crosslinked network in which some phosphate units are entrapped, as we previously observed for NbPSi dried gels [27]. When Ti is substituted by Zr, the yield of hydrolysis and cross-condensation reactions seems to increase, probably due to the higher reactivity of Zr alkoxide and the different Me/*Hacac*/*AcOH* molar ratios adopted in the synthesis, forming a Si–O–Zr–O–P crosslinked network with a larger extent of phosphate groups coordination. This structural difference mirrors in the samples treated at 500 °C. Concerning ZrPSi, only a slight change of the intensity distribution occurs, with an increase in the less shielded components of the spectrum. Conversely, for TiPSi the curve broadens and the signals at larger chemical shift increase in intensity, keeping almost unchanged the Q'_0 resonance (Fig. 3 and Table 1). These results indicate that the thermal treatment promotes a different evolution of the chemical structure of the xerogels, depending mainly on the kind of metal. Upon heating two counteracting effects occur: the degradation and complete removal of the organic components and the typical dehydroxylation with loss of water and increase of polymerization degree [52]. The apparent partial depolymerization observed for the sample containing Zr may be ascribed to combined effects of the evacuation of complexing agents (*acac* and acetate), that can destabilize some Zr–O–P cross-links, and the high content of –OH groups still present after the heat treatment (see below), whose stability hampers further condensation. Indeed, in the case of Ti the dehydroxylation prevails, favouring the formation of new metal-phosphate linkages, possibly supported by a higher acidity of Ti^{4+} than Zr^{4+} ions. Surprisingly, this evolution does not involve the Q'_0 units that appear stably trapped in the framework.

The FTIR spectra of the dried and calcined gels are shown in Fig. 4a. The strong, asymmetric band centred at 1074 cm^{-1} is characteristic of Si–O bonds stretching in a silicate framework and the absorption bands at about 450 and 795 cm^{-1} are assigned respectively to the symmetric bending and stretching of Si–O–Si bonds. The vibrations of P–O and P═O bonds in phosphate species are expected to be mostly overlapped to the abovesaid Si-related features [59], as confirmed by the spectra of TiP or ZrP materials reported in the literature [7,13], so they cannot be clearly observed. The band at 950 cm^{-1}, well-resolved only in TiPSi samples, can be ascribed to Ti–O–Si bonds [12,60,61]. This attribution is supported by the absence of this band in ZrPSi samples, where it becomes a shoulder, as Zr–O–Si vibrations are supposed to be found at slightly higher wavenumbers [62]. On the other side, the growth of a component around 960 cm^{-1} can also be due to the Si–OH stretching mode [63] in agreement with the detection of isolated silanol in the pure powder spectra, as discussed below. Finally, the weak features seen at about 2950, 1700, 1540 and 1360 cm^{-1} in the xerogels are linked to the *acac*, acetate and alkoxide ligands that are still bound in the structure and then removed by heating.

FTIR spectra of pure powders in the OH stretching region are reported in Fig. 4b. The sharp band at 3741 cm^{-1}, detected in the spectrum of sample ZrPSi, is assigned to isolated silanol groups [64]. A small shoulder around 3730 cm^{-1} could suggest the formation of another family of silanol groups likely interacting with nearby electron-withdrawing atoms. The broad and intense absorption band tailing to lower frequencies is associated with O–H stretching modes of hydroxyl groups involved in hydrogen bond interactions. In both samples, IR spectra show a highly hydroxylated surface even after the thermal treatment. Apparently, no isolated silanols are detected in the spectra of TiPSi sample, suggesting a strong interaction among all the exposed hydroxyl groups, regardless of the different chemical nature. For the same reason, isolated P–OH species, characterized by a band in the range 3665-3650 cm^{-1}, cannot be detected in these samples after activation at high temperature (see reference PSi spectrum in Fig. 4b) [31]. Moreover, the amount of exposed P–OH groups is indeed limited by the crosslinking occurring to form Si–O–Me–O–P species, as discussed above. A representative structure of the ternary oxide network, based on the NMR and FTIR data, is illustrated in Fig. 5.

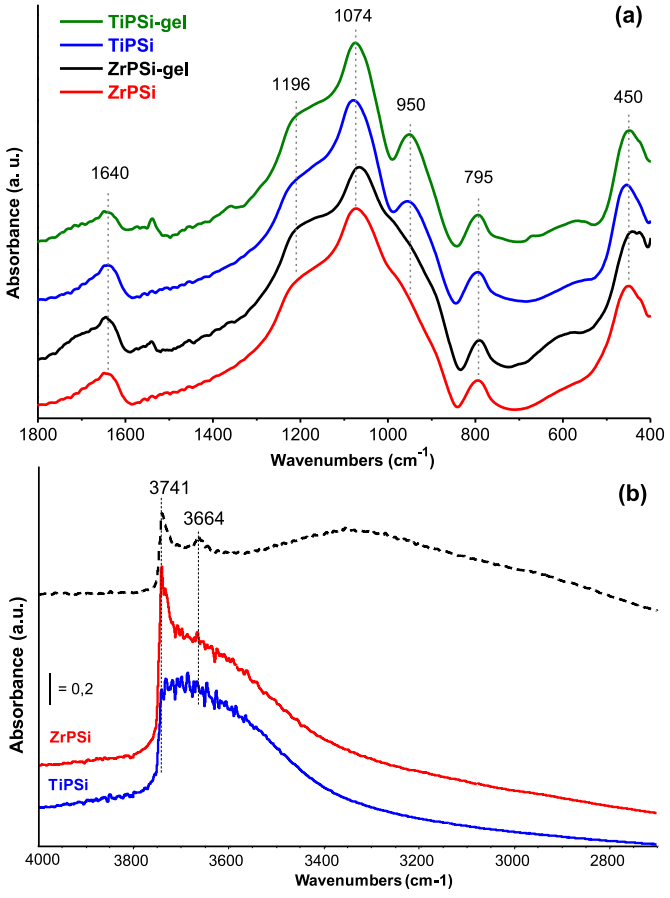

Fig. 4. FTIR spectra of (a) as-prepared samples diluted in KBr and (b) pure powder activated samples (OH stretching region). Dashed line: spectrum of PSi sample as reference.

3.4. Surface characterization

The chemical composition of TiPSi and ZrPSi surfaces was analysed by X-ray photoelectron spectroscopy (XPS). Surface composition, as determined by XPS, was compared to nominal bulk composition to unravel possible surface enrichment or depletion effects. Table 2 gathers surface composition in terms of atomic concentrations (at.%) and atomic ratios. The ZrPSi sample has almost twice the surface concentration of metal (Zr, 2.7 at.%) as the TiPSi sample (Ti, 1.5 at.%), although they are supposed to have the same bulk composition (see Table S2). The different metal content at the surface might be ascribed to rearrangements and migration of atoms from the surface to the bulk or vice-versa, occurring during the calcination and leading to differences in the amounts of metal in the surface layers. The comparison between surface and bulk compositions, revealed that surface Si/Me ratios (19.3 for Si/Ti and 11.0 for Si/Zr) deviate considerably from the nominal bulk ratio values (8.7), suggesting that Si is enriched at the surface, while the metal components (Zr or Ti) are depleted. It is worth noting that the P/Me ratio remains the same in both samples, which can be regarded as another hint at their association, suggested by solid state NMR data.

Surface area and porosity were determined by N_2 adsorption-desorption isotherms. The collected isotherms are reported in Fig. 6 and reveal the microporous nature of both TiPSi and ZrPSi samples, in agreement with previous investigation carried out on niobium-containing ternary oxides prepared through a similar sol-gel procedure [31]. Specific surface area and pore volume values are listed in Table 3. Slightly higher surface area values for TiPSi (between 395 and 441 $m^2\ g^{-1}$) than ZrPSi (between 346 and 421 $m^2\ g^{-1}$) were computed according to Brunauer–Emmett–Teller (BET) and Langmuir model equations; the latter is more appropriate for modelling the surface of microporous solids. The two samples show similar pore volumes (ca. 0.2 $cm^3\ g^{-1}$) and pore size distributions dominated by small micropores, as determined by Horvath Kawazoe model. In fact, in both cases 75 % of pore volume was associated with pores having diameter <2 nm, while 20 % was constituted by pores with size between 2 and 6 nm and only 5 % of pore volume derives from pores with diameters in the 6–10 nm range. The specific surface areas and pore volumes are comparable to those reported for different Ti–P–Si ternary oxides prepared without templates (see Table S4).

The nature and strength of acid sites exposed at the catalyst surface and their relative abundance is a key factor in the evaluation of the catalytic activity. As for the binary TiP and ZrP materials, in the open literature there is a general agreement that coordinatively unsaturated zirconium and titanium ions behave as medium-strength Lewis sites. Modification with phosphate leads to the additional appearance of Brønsted acidity due to exposed monohydrogen phosphate groups, and the enhancement of such acidity has been related to the increase in P content, and therefore to the increase of terminal P–OHs [4,12,13,63]. Stegmann et al. also reported on the key role of activation with water (added to the feed or produced by the reaction itself) that adsorbs dissociatively on the TiP catalyst surface by breaking Ti–O–P and P–O–P bonds, thus forming more Ti–OH and P–OH acidic groups [65]. As discussed in the previous paragraphs, in the silica-based ternary formulations the surface is additionally characterized by exposed silanol groups involved in extensive H-bonds, thus suggesting a quite complex acidic behaviour. In the following section, FTIR studies of pyridine (PY)

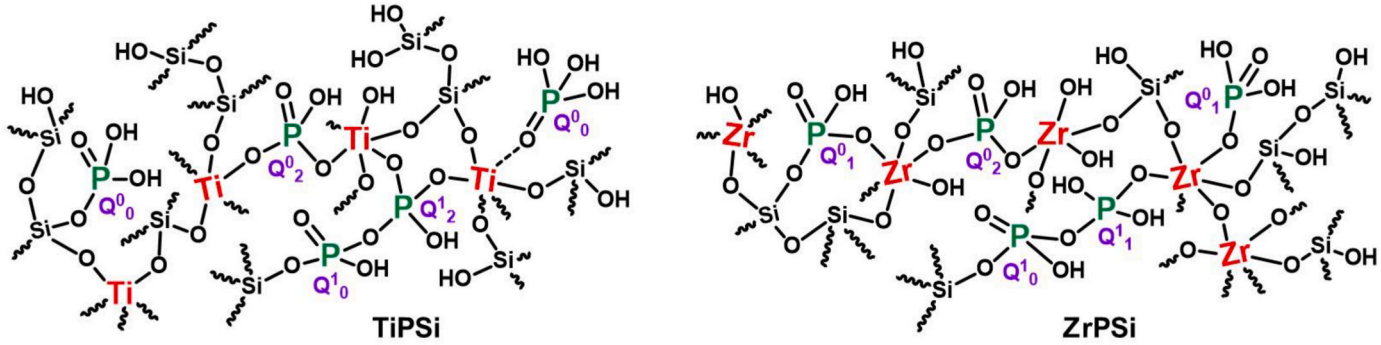

Fig. 5. Illustrative representation of the surface structure of TiPSi and ZrPSi gel-derived oxides, based on solid state NMR, FTIR and XPS results. For P atoms, the corresponding Q^n_m notation is indicated, where n and m represent the number of linkages with P and Me atoms, respectively.

Table 1
Chemical shifts, δ (ppm), estimated relative intensities, and full width at half maximum, FWHM (ppm), calculated from line fitting of ^{29}Si and ^{31}P solid state NMR spectra. Standard errors are reported in parentheses.

Sample	^{29}Si			^{31}P		
	δ (ppm)	Relative Area	FWHM (ppm)	δ (ppm)	Relative Area	FWHM (ppm)
ZrPSi-gel	−91.02 (0.02)	0.092 (0.001)	6.01 (0.06)	−12.60 (0.08)	0.143 (0.003)	9.02 (0.09)
	−99.44 (0.01)	0.445 (0.002)	6.54 (0.02)	−17.07 (0.02)	0.082 (0.003)	5.41 (0.05)
	−107.66 (0.02)	0.463 (0.002)	8.76 (0.03)	−22.53 (0.01)	0.775 (0.002)	10.33 (0.01)
ZrPSi	−90.21 (0.04)	0.077 (0.001)	6.79 (0.07)	−13.7 (0.2)	0.32 (0.01)	13.5 (0.1)
	−98.83 (0.02)	0.30 (0.001)	7.75 (0.05)	−18.61 (0.03)	0.027 (0.002)	5.6 (0.1)
	−107.36 (0.02)	0.62 (0.001)	10.44 (0.03)	−23.0 (0.1)	0.65 (0.01)	15.93 (0.08)
TiPSi-gel	−90.81 (0.01)	0.079 (0.001)	5.38 (0.03)	−1.80 (0.06)	0.143 (0.005)	9.66 (0.05)
	−99.82 (0.01)	0.449 (0.001)	6.47 (0.01)	−10.44 (0.02)	0.640 (0.008)	12.5 (0.1)
	−108.57 (0.01)	0.472 (0.001)	8.23 (0.02)	−21.58 (0.07)	0.217 (0.004)	12.25 (0.06)
TiPSi	−90.70 (0.03)	0.069 (0.001)	6.39 (0.07)	−2.95 (0.06)	0.151 (0.004)	12.07 (0.05)
	−99.17 (0.01)	0.282 (0.002)	7.13 (0.04)	−13.38 (0.04)	0.42 (0.01)	15.5 (0.2)
	−107.92 (0.01)	0.649 (0.002)	10.15 (0.02)	−25.3 (0.1)	0.427 (0.007)	16.97 (0.07)

Table 2
Surface composition of calcined samples as determined by XPS.

Sample	Survey composition (at %)				Surface ratio		Bulk ratio[a]	
	Si	O	Me	P	Si/Me	P/Me	Si/Me	P/Me
TiPSi	29.3	68.6	1.5	0.6	19.3	0.4	8.7	0.5
ZrPSi	29.3	67.0	2.7	1.0	11.0	0.4	8.7	0.5

[a] Nominal composition from the synthesis data.

adsorption and its desorption at increasing temperatures will assess the surface acidity of these materials.

The subtraction spectra of surface species arising from PY adsorption on ZrPSi sample are reported in Fig. 7a. After adsorption and desorption at room temperature both Brønsted acidity and Lewis acidity are detected, characterized by pyridinium ion (8a band at 1638 cm^{-1} and 19b band at 1545 cm^{-1}) and coordinated pyridine (8a band at 1608 cm^{-1} and 19b band at 1446 cm^{-1}) [66]. H-bonded species are characterized by the band at 1596 cm^{-1} (8a) and disappear after outgassing between room temperature and 150 °C. Upon heating, the band diagnostic of Lewis acidity is predominant in the spectra up to over 350 °C. Correspondingly, in the high frequency region of the spectrum, hydroxyl groups involved in the H bonds appear as negative band and a broad band shifted to lower frequencies (Figure S5). Interestingly, the band due to silanol species is split into two negative components at 3741 (isolated silanols) and 3732 cm^{-1}. This would confirm the presence of two families of silanols, one of them having higher acidity due to the interaction with nearby atoms.

Similar features can be detected in the spectra of surface species from PY adsorption over TiPSi sample (Fig. 7b). At room temperature, the band at 1544 cm^{-1} and the shoulder at 1638 cm^{-1} are due to pyridine protonated by Brønsted acidic sites. These components become more defined following outgassing from 150 up to 300 °C. In the same temperature range, the shoulder detected at 1607 cm^{-1} and due to PY coordinated over Lewis sites, becomes a sharp band. At high temperatures this peak is the most evident in the spectrum, together with a component at 1446 cm^{-1}. From the IR results, it is clear that the presence of Zr or Ti induces the formation of surface Lewis sites, corresponding to exposed, coordinatively unsaturated metal ions [67,68]. The frequency of the PY 8a band, 1608-1609 cm^{-1}, is typical of medium strength electron-withdrawing sites. It is worthy of note that, in the spectrum of PY adsorbed over ZrPSi sample, the shoulder due to PY over Lewis sites is already more evident at room temperature than in the spectrum of TiPSi sample. This effect is consistent with XPS results pointing out a relative enrichment of metal sites at the catalyst surface in the case of Zr. The lower Si/Me ratio could also explain the presence of isolated silanols typical of this surface, where the H-bonds among exposed silanols are somehow limited by the presence of exposed Zr^{4+} ions. On the other side, the higher ratio Si/Ti could lead to the formation of isles of exposed silanols strongly interacting with each other. In both formulations, the strong Brønsted acidity mainly arises from exposed P–OH groups, as pure silica is unable to protonate PY. Pyridine adsorption has also been carried out over the binary PSi system, synthetized as reference material. In the spectrum reported in Fig. 7a (dashed line), no bands due to Lewis sites could be detected at about 1600 cm^{-1}, while components at 1639 and 1548 cm^{-1} characterize the pyridinium ion formed by interaction with Brønsted sites, in agreement with previous assignment over the ternary systems. The study of the high frequency region of the spectra shows that after PY interaction, and pyridinium ion formation, both Si–OH and P–OH bands decrease in intensity, but silanol groups are apparently more affected than P–OH groups (Figure S6). Considering these results, we can also suggest the formation of a fraction of silanol groups whose acidity is increased by the interaction with adjacent P atoms having high electronegativity and variable coordination state. This effect can also occur at the surface of ternary oxides where the interaction of silanol with exposed metal ions might lead to the formation of pseudo-bridging silanol type structure, in addition to the strongly acidic P–OH groups. Such a structure has been reported to be able to protonate pyridine molecule. Very recently, Wolek et al. described the same effect to occur after silica deposition over Lewis acidic oxides,

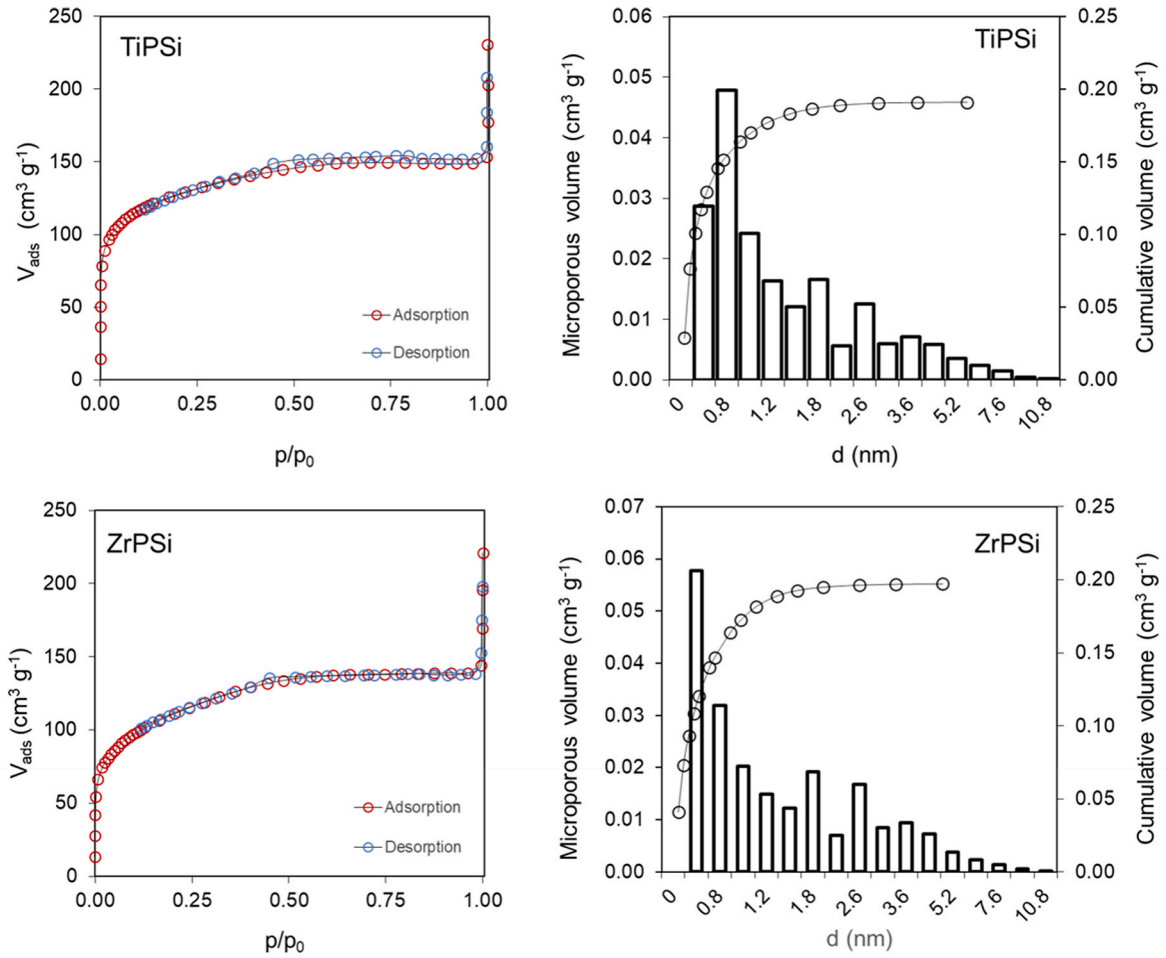

Fig. 6. N_2 adsorption and desorption isotherms at −196 °C (left panels) and cumulative pore volume with pore size distribution determined by Horvath Kawazoe model equation (right panels) of calcined samples.

Table 3
Specific surface area (SSA, m^2 g^{-1}), micropore volume (cm^3 g^{-1}) and total acidity (expressed as acid sites number, μmol g^{-1}) of the calcined samples.

Sample	SSA (m^2 g^{-1})		Microporous volume (cm^3 g^{-1})[b]	Surface acid sites (μeq g^{-1})[c]	Acid site density (μeq m^{-2})
	BET[a]	Langmuir			
TiPSi	395 ± 11	441 ± 10	0.19 ± 0.02	744[d]	1.7
ZrPSi	346 ± 37	421 ± 20	0.21 ± 0.03	702[d]	1.7

[a] Evaluated by 3-parameter BET, pressure range $0.005 < p/p_0 < 0.4$.
[b] Cumulative pore volume obtained by Horvath Kawazoe model, pressure range $0.0 < p/p_0 < 0.35$ applied on adsorption branch.
[c] Measured by gas–solid phase titrations with NH_3 probe at T = 80 °C.

including ZrO_2 and TiO_2. The strength of the newly formed acidic sites was related to the Lewis acidity of the metal ions, thus the strength of the Brønsted centres was in the order: $SiO_2/Al_2O_3 > SiO_2/Nb_2O_5 > SiO_2/TiO_2 > SiO_2/ZrO_2$ [69]. While a similar effect of Zr ions has been noted also over zirconium-doped mesoporous silica [63], the effect of Ti ions is controversial: no evidence of pyridinium ion has been reported on coprecipitated SiO_2–TiO_2 mixed oxides, although in any case stronger acidic silanol groups were detected on the samples containing both silica and titania and probed by pivalonitrile adsorption [70].

Following these findings, we also evaluated the resistance of adsorbed species to outgassing as an indication of the strength of surface acidity. At increasing temperature, features due to PY over Brønsted and Lewis sites decreased in intensity on both samples. In Figure S7, the plot of PYH^+ band intensity is reported as normalized integrated area versus temperature [71] and the trend evidences how PY desorption is slightly faster on ZrPSi sample than on TiPSi, namely above 200 °C. A small fraction of adsorbed PY (10 % ca.) is actually still detectable at the TiPSi surface following desorption at 400 °C, likely evidencing a stronger Brønsted acidity of this catalyst.

As reported in previous papers [31,72] the adsorption of the pyridine probe has been carried out also on the "wet" surface, i.e. a surface that has been submitted to hydration in contact with water vapor at room temperature (Fig. 8). In this experiment, both Brønsted and Lewis acidic sites are detected, showing that the stronger base (PY) is able to displace water molecules from acidic sites [73]. Thus, the adsorption of water vapor in small amount does not change the acidic character of the surfaces.

Subsequently, surface acidity of the two TiPSi and ZrPSi samples was quantified by gas-solid titrations. Considering the microporous nature of the samples, the total number of acid sites was titrated using ammonia as a basic probe molecule, able to access micropores and interact with acid sites exposed at both external and internal surfaces. TiPSi and ZrPSi showed similar acid character with similar acid site density (Table 3), despite the different surface metal content as revealed by XPS (Table 2). It is then possible to assume that the acid character of the surfaces is mainly ascribable to Si–OH (whose acidity might be enhanced by nearby metal ions), and P–OH groups, in agreement with FTIR data of adsorbed pyridine. The Lewis sites corresponding to the exposed metal ions would contribute to the overall acidic character in a similar and limited extent over the two catalysts.

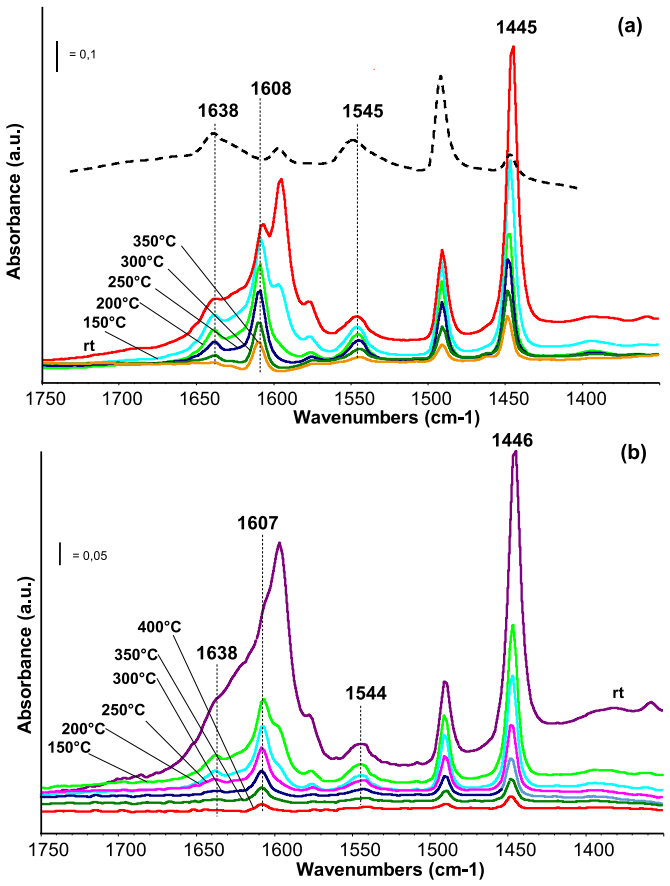

Fig. 7. FTIR spectra of surface species arising from adsorption/desorption of PY over (a) ZrPSi and (b) TiPSi. The activated surface has been subtracted. Dashed line: PY adsorbed and desorbed at 130 °C over the reference PSi sample.

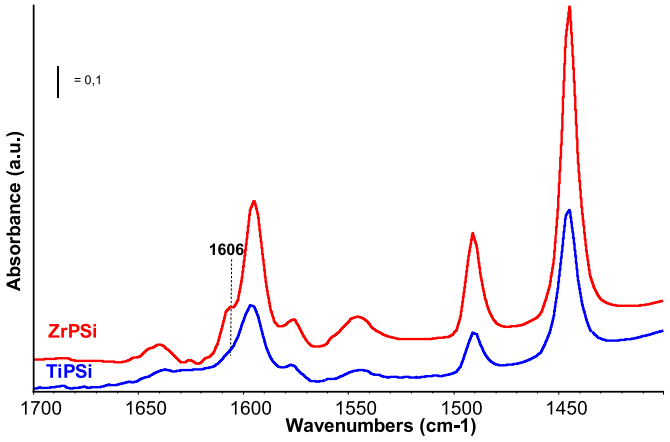

Fig. 8. FTIR spectra of surface species arising from pyridine adsorption/desorption at room temperature. The activated surface has been subtracted.

3.5. Surface reactivity

The acidic features of the TiPSi and ZrPSi surfaces, with predominant Brønsted acid sites over Lewis sites, can justify their application as heterogeneous acid catalysts. Sucrose hydrolysis to glucose and fructose was selected as a model reaction to evaluate the surface reactivity of the samples. Indeed, the hydrolysis of disaccharides in water excess is considered a pseudo-first order reaction. Sucrose molecule has glucosidic and fructosidic units linked by α-1,β-2 glycosidic bond, which requires Brønsted acid sites to be cleaved (Scheme 2). In particular, acid catalysts must possess labile protons with sufficient mobility to reach the oxygen of the acetal bonds and promote the hydrolysis. The most established mechanism, which holds on to purely acidic surfaces, begins with the adsorption of sucrose using oxygen electron lone pairs or hydroxyl groups, followed by protonation of the oxygen atom involved in the ether linkage. Then, a water molecule is inserted, causing the breaking of the C–O bond (Scheme S1). Thus, the catalytic activity towards the sucrose unit is expected to be strongly dependent on the nature (Brønsted or Lewis) and strength of the surface acid sites.

The reaction tests were carried out in a batch reactor while the temperature was increased from 50 to 90 °C at 0.12 °C/min heating rate. The non-isothermal operative mode is suitable for rapid screening of catalytic activity, allowing evaluation of the conversion and average reaction rates as a function of temperature and time. The temperature window for screening was limited to 90 °C to minimize secondary reactions, as dehydration or humin formation.

The fully hydroxylated surface of the two materials proved to be active in the hydrolysis reaction of sucrose. The samples were active in the temperature window between 60 and 80 °C as already reported for other organic and inorganic solid acid catalysts (e.g. Amberlite resins, niobium phosphate and niobium oxide). Fig. 9 reports the conversion reached for the two samples at the end of the temperature program (i.e. at attainment of 90 °C), which is between 35 and 40 %. These conversion values were lower compared to the most active organic and inorganic solid acid catalysts. However, a direct comparison of the observed catalytic performances is not straightforward due to differences in reactor configuration (batch vs. flow reactors) and operating conditions (temperature, catalyst/sucrose mass ratio, sucrose initial concentration). Among zeolite topologies (H–Y, H-MOR, H-BEA, H-BETA, H-ZSM5), H–Y zeolite demonstrated the most notable performance, achieving sucrose conversions of 90–100 % even at low temperatures (90–100 °C). Similar performance was observed with organic resins (Amberlite and Amberlyst). Interestingly, when considering other oxidic materials, the added value of ternary materials became apparent. For instance, SiO_2–ZrO_2 reached only 11 % sucrose conversion at 80 °C, indicating that the incorporation of phosphate in the formulation (SiZrP) significantly increased the catalytic performance.

The average rate of sucrose conversion was higher for TiPSi than for ZrPSi, indicating the presence of acid sites with higher average strength in the former sample, consistent with IR data from adsorbed pyridine. Activation parameters were determined using an Arrhenius-like approach (see Figure S2). Comparative evaluation of the activation energy and pre-exponential factor (refer to Table S3) revealed similar activation parameters for both catalysts, approximately 78 kJ mol^{-1} for E_a and around 24 for ln A. These values compare well with those of anionic organic resins (such as Amberlite A120) but are lower than those exhibited by inorganic oxides like SiO_2–Al_2O_3, SiO_2–ZrO_2, and Nb_2O_5 (with E_a values falling in the range of 120–130 kJ mol^{-1}). This finding confirms the superior activity of the studied ternary oxides over the mentioned inorganic oxides.

In both cases, the reaction proceeded with complete selectivity to glucose and fructose, without the formation of secondary products from dehydration reactions, which could be promoted by cooperation between Brønsted and Lewis acid sites; likely, the dehydration reaction would necessitate higher temperatures to occur.

4. Conclusions

A straightforward sustainable synthetic route was developed to obtain silica-based solids with phosphorus and either titanium or zirconium dispersed in the network at the molecular scale. Through a careful choice of the raw materials and process parameters, energy-efficient protocols were established, allowing for a fine control of the precursors' reactivity and the production of homogeneous amorphous gels. The simple and complete E factors estimated for the preparation of

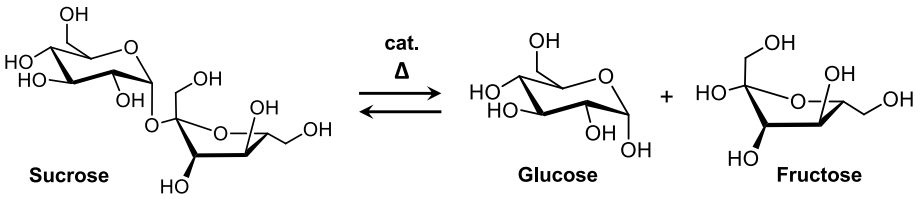

Scheme 2. Sucrose hydrolysis reaction.

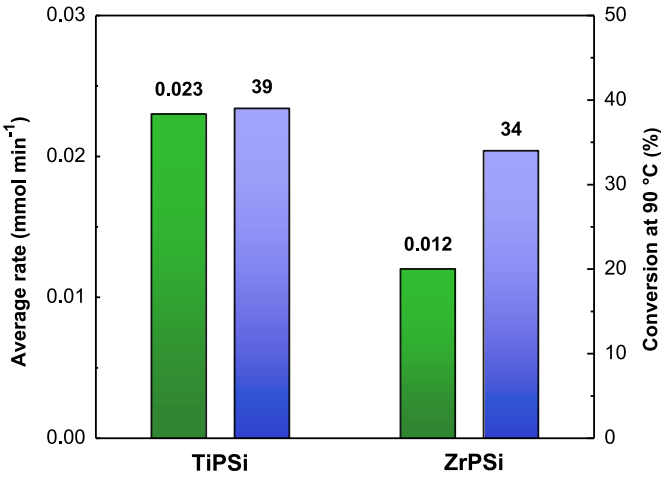

Fig. 9. Results of sucrose hydrolysis reaction tests: average rate after 240 min reaction when temperature attained 80 °C starting from 50 °C at increasing rate of 0.12 °C/min (green bars) and conversion attained at 90 °C (blue bars). (For interpretation of the references to colour in this figure legend, the reader is referred to the Web version of this article.)

the Ti–P–Si material are 3.6 and 9.4, respectively, and the values are even lower for Zr–P–Si oxide. The E factors are significantly reduced compared to most of the values calculated for the synthesis of similar materials. These data prove an excellent mass intensity, that is, a limited waste of matter in the process.

In the oxide frameworks, both metals are found to be associated to phosphorus, either through P–O–Me–O–Si linkages or by coordination of phosphate groups. On the other hand, they affect the chemical environment and distribution of phosphorus in different ways, particularly titanium induces a wider variety of P connectivity and more Si surface enrichment compared to zirconium. Hydroxy groups of different acidic strength are exposed at the catalyst surface and contribute to the overall acidity of the catalyst: weakly acidic silanol groups, Brønsted acidic P–OH groups and possibly pseudo-bridging silanol groups whose acidity is increased by the nearby electron-withdrawing atoms. Moreover, Lewis sites are associated to the presence of exposed coordinatively unsaturated Zr and Ti ions. A preliminary catalytic assessment in the hydrolysis of sucrose confirmed their activity, indicating a faster reaction rate over the Ti–P–Si ternary oxide, in agreement with the slightly higher acid strength and surface amount of acid sites detected on this sample.

The proposed sol-gel strategy may be a reference point for the design of the green synthesis of acid solids with variable metal content and phosphorus distribution, hence with tuneable type and strength of acid sites and a controlled surface composition and porosity. These results are envisaged to inspire further studies addressing the dispersion of metal phosphates in porous host matrices, for applications in adsorption, acid catalysis, proton exchange, and related processes.

Funding sources

This study was partially supported by the Agritech National Research Center and received funding from the European Union Next-GenerationEU (Piano Nazionale di Ripresa e Resilienza (PNRR) – Missione 4 Componente 2, Investimento 1.4 – D.D. 1032 June 17, 2022, CN00000022). This manuscript reflects only the authors' views and opinions, neither the European Union nor the European Commission can be considered responsible for them.

CRediT authorship contribution statement

Claudio Imparato: Writing – review & editing, Methodology, Investigation, Formal analysis, Conceptualization. **Elisabetta Finocchio:** Writing – review & editing, Methodology, Investigation, Formal analysis. **Sebastiano Campisi:** Writing – review & editing, Investigation, Formal analysis. **Michele Bigica:** Investigation, Formal analysis. **Antonella Gervasini:** Writing – review & editing, Supervision, Conceptualization. **Aurelio Bifulco:** Writing – review & editing, Methodology, Investigation, Conceptualization. **Roberto Avolio:** Writing – review & editing, Methodology, Investigation, Formal analysis. **Nigel J. Clayden:** Writing – review & editing, Formal analysis. **Maria E. Errico:** Writing – review & editing, Methodology, Investigation, Formal analysis. **Antonio Aronne:** Writing – review & editing, Supervision, Conceptualization.

Declaration of competing interest

The authors declare that they have no known competing financial interests or personal relationships that could have appeared to influence the work reported in this paper.

Data availability

Data will be made available on request.

Appendix A. Supplementary data

Supplementary data to this article can be found online at https://doi.org/10.1016/j.mtchem.2024.102126.

References

[1] P. Bhanja, J. Na, T. Jing, J. Lin, T. Wakihara, A. Bhaumik, Y. Yamauchi, Nanoarchitectured metal phosphates and phosphonates: a new material horizon toward emerging applications, Chem. Mater. 31 (2019) 5343–5362, https://doi.org/10.1021/acs.chemmater.9b01742.
[2] T. Kimura, An opportunity for utilizing earth-abundant metals through the mesostructural design of metal phosphate-based materials, J. Mater. Chem. A 8 (2020) 25528–25547, https://doi.org/10.1039/d0ta09419f.
[3] A. Clearfield, D.S. Thakur, Zirconium and titanium phosphates as catalysts: a review, Appl. Catal. 26 (1986) 1–26, https://doi.org/10.1016/S0166-9834(00)82538-5.
[4] S. Yadav, N. Beniwal, P. Rekha, L. Singh, Recent advances in the synthesis and applications of porous zirconium phosphate, J. Porous Mater. 29 (2022) 1707–1725, https://doi.org/10.1007/s10934-022-01286-2.
[5] F. Benvenuti, C. Carlini, P. Patrono, A.M. Raspolli Galletti, G. Sbrana, M. A. Massucci, P. Galli, Heterogeneous zirconium and titanium catalysts for the selective synthesis of 5-hydroxymethyl-2-furaldehyde from carbohydrates, Appl. Catal. Gen. 193 (2000) 147–153, https://doi.org/10.1016/S0926-860X(99)00424-X.
[6] S.K. Das, M.K. Bhunia, A.K. Sinha, A. Bhaumik, Synthesis, characterization, and biofuel application of mesoporous zirconium oxophosphates, ACS Catal. 1 (2011) 493–501, https://doi.org/10.1021/cs200005z.

[7] V.V. Ordomsky, V.L. Sushkevich, J.C. Schouten, J. Van Der Schaaf, T.A. Nijhuis, Glucose dehydration to 5-hydroxymethylfurfural over phosphate catalysts, J. Catal. 300 (2013) 37–46, https://doi.org/10.1016/j.jcat.2012.12.028.

[8] P. Carniti, A. Gervasini, F. Bossola, V. Dal Santo, Cooperative action of Brønsted and Lewis acid sites of niobium phosphate catalysts for cellobiose conversion in water, Appl. Catal. B Environ. 193 (2016) 93–102, https://doi.org/10.1016/J.APCATB.2016.04.012.

[9] G. Gliozzi, A. Innorta, A. Mancini, R. Bortolo, C. Perego, M. Ricci, F. Cavani, Zr/P/O catalyst for the direct acid chemo-hydrolysis of non-pretreated microcrystalline cellulose and softwood sawdust, Appl. Catal. B Environ. 145 (2014) 24–33, https://doi.org/10.1016/J.APCATB.2012.12.035.

[10] C. Antonetti, M. Melloni, D. Licursi, S. Fulignati, E. Ribechini, S. Rivas, J.C. Parajó, F. Cavani, A.M. Raspolli Galletti, Microwave-assisted dehydration of fructose and inulin to HMF catalyzed by niobium and zirconium phosphate catalysts, Appl. Catal. B Environ. 206 (2017) 364–377, https://doi.org/10.1016/j.apcatb.2017.01.056.

[11] T. Fovanna, S. Campisi, A. Villa, A. Kambolis, G. Peng, D. Rentsch, O. Kröcher, M. Nachtegaal, D. Ferri, Ruthenium on phosphorous-modified alumina as an effective and stable catalyst for catalytic transfer hydrogenation of furfural, RSC Adv. 10 (2020) 11507–11516.

[12] W. Guo, E.J.M. Hensen, W. Qi, H.J. Heeres, J. Yue, Titanium phosphate grafted on mesoporous SBA-15 silica as a solid acid catalyst for the synthesis of 5-hydroxymethylfurfural from glucose, ACS Sustain. Chem. Eng. 10 (2022) 10157–10168, https://doi.org/10.1021/acssuschemeng.2c01394.

[13] F. Li, L.J. France, Z. Cai, Y. Li, S. Liu, H. Lou, J. Long, X. Li, Catalytic transfer hydrogenation of butyl levulinate to Γ-valerolactone over zirconium phosphates with adjustable Lewis and BrØnsted acid sites, Appl. Catal. B Environ. 214 (2017) 67–77, https://doi.org/10.1016/j.apcatb.2017.05.013.

[14] A. Dutta, A.K. Patra, S. Dutta, B. Saha, A. Bhaumik, Hierarchically porous titanium phosphate nanoparticles: an efficient solid acid catalyst for microwave assisted conversion of biomass and carbohydrates into 5-hydroxymethylfurfural, J. Mater. Chem. 22 (2012) 14094–14100, https://doi.org/10.1039/c2jm30623a.

[15] R. Weingarten, Y.T. Kim, G.A. Tompsett, A. Fernández, K.S. Han, E.W. Hagaman, W.C. Conner, J.A. Dumesic, G.W. Huber, Conversion of glucose into levulinic acid with solid metal(IV) phosphate catalysts, J. Catal. 304 (2013) 123–134, https://doi.org/10.1016/j.jcat.2013.03.023.

[16] G. Zhang, W. Xie, ZrMo oxides supported catalyst with hierarchical porous structure for cleaner and sustainable production of biodiesel using acidic oils as feedstocks, J. Clean. Prod. 384 (2023) 135594, https://doi.org/10.1016/j.jclepro.2022.135594.

[17] W. Xie, Q. Wang, L. Guo, Q. Zhang, Improved biodiesel production from soybean oil using molybdenum-zirconium doped aluminosilicates as heterogeneous catalysts, BioEnergy Res 17 (2024) 532–546, https://doi.org/10.1007/s12155-023-10662-y.

[18] T. Uma, S. Izuhara, M. Nogami, Structural and proton conductivity study of P_2O_5-TiO_2-SiO_2 glasses, J. Eur. Ceram. Soc. 26 (2006) 2365–2372, https://doi.org/10.1016/j.jeurceramsoc.2005.04.013.

[19] J. Mosa, G. Larramona, A. Durán, M. Aparicio, Synthesis and characterization of P_2O_5-ZrO_2-SiO_2 membranes doped with tungstophosphoric acid (PWA) for applications in PEMFC, J. Memb. Sci. 307 (2008) 21–27, https://doi.org/10.1016/j.memsci.2007.06.035.

[20] J. Zhang, Z. Ma, J. Jiao, H. Yin, W. Yan, E.W. Hagaman, J. Yu, S. Dai, Layer-by-layer grafting of titanium phosphate onto mesoporous silica SBA-15 surfaces: synthesis, characterization, and applications, Langmuir 25 (2009) 12541–12549, https://doi.org/10.1021/la9017486.

[21] J. Zhang, Z. Ma, J. Jiao, H. Yin, W. Yan, E.W. Hagaman, J. Yu, S. Dai, Surface functionalization of mesoporous silica SBA-15 by liquid-phase grafting of zirconium phosphate, Microporous Mesoporous Mater. 129 (2010) 200–209.

[22] A.A.S. Alfaya, Y. Gushikem, S.C. De Castro, Highly dispersed phosphate supported in a binary silica-titania matrix: preparation and characterization, Chem. Mater. 10 (1998) 909–913, https://doi.org/10.1021/cm970679e.

[23] A.A.S. Alfaya, Y. Gushikem, S.C.D. Castro, Silica-zirconia-phosphate composites: a study of their synthesis, proton exchange capacity and ammonia gas adsorption, Microporous Mesoporous Mater. 39 (2000) 57–65, https://doi.org/10.1016/S1387-1811(00)00176-1.

[24] T.V. Kovalchuk, H. Sfihi, A.S. Korchev, A.S. Kovalenko, V.G. Il'in, V.N. Zaitsev, J. Fraissard, Synthesis, structure, and acidic properties of MCM-41 functionalized with phosphate and titanium phosphate groups, J. Phys. Chem. B 109 (2005) 13948–13956, https://doi.org/10.1021/jp0580625.

[25] N.J. Clayden, G. Accardo, P. Mazzei, A. Piccolo, P. Pernice, A. Vergara, C. Ferone, A. Aronne, Phosphorus stably bonded to a silica gel matrix through niobium bridges, J. Mater. Chem. A 3 (2015) 15986–15995, https://doi.org/10.1039/C5TA03267A.

[26] S.N. Antonio de Brito, A.C. Oliveira, S. Mishra, N. Essayem, Sol-Gel controlled dispersion of Nb within TiO_2 to obtain water tolerant catalysts with tunable acid-base properties for dihydroxyacetone transformation, Appl. Catal. Gen. 658 (2023) 119165.

[27] N.J. Clayden, C. Imparato, R. Avolio, G. Ferraro, M.E. Errico, A. Vergara, G. Busca, A. Gervasini, A. Aronne, B. Silvestri, Chloride-free hydrolytic sol-gel synthesis of Nb-P-Si oxides: an approach to solid acid materials, Green Chem. 22 (2020) 7140–7151, https://doi.org/10.1039/d0gc02519d.

[28] A. Aronne, M. Di Serio, R. Vitiello, N. Clayden, L. Minieri, C. Imparato, A. Piccolo, P. Pernice, P. Carniti, A. Gervasini, An Environmentally Friendly Nb–P–Si Solid Catalyst for Acid-Demanding Reactions, J. Phys. Chem. C 121 (n.d.) 17378–17389. https://doi.org/10.1021/acs.jpcc.7b05886.

[29] A. Gervasini, P. Carniti, F. Bossola, C. Imparato, P. Pernice, N.J. Clayden, A. Aronne, New Nb-P-Si ternary oxide materials and their use in heterogeneous acid catalysis, Mol. Catal. 458 (2018) 280–286, https://doi.org/10.1016/j.mcat.2017.10.006.

[30] A. Gervasini, S. Campisi, P. Carniti, M. Fantauzzi, C. Imparato, N.J. Clayden, A. Aronne, A. Rossi, Influence of the Nb/P ratio of acidic Nb-P-Si oxides on surface and catalytic properties, Appl. Catal. Gen. 579 (2019) 9–17, https://doi.org/10.1016/j.apcata.2019.04.008.

[31] G. Garbarino, G. Pampararo, E. Finocchio, G. Busca, A. Gervasini, S. Campisi, B. Silvestri, C. Imparato, A. Aronne, Surface acid properties of Nb_2O_5–P_2O_5–SiO_2 gel-derived catalysts, Microporous Mesoporous Mater. 343 (2022) 112190, https://doi.org/10.1016/j.micromeso.2022.112190.

[32] M. Paul, N. Pal, M. Ali, A. Bhaumik, New mesoporous silicotitaniumphosphate and its application in acid catalysis and adsorption of As(III/V), Cd(II) and Hg(II), J. Mol. Catal. Chem. 330 (2010) 49–55, https://doi.org/10.1016/j.molcata.2010.07.001.

[33] G. Busca, Infrared (IR) spectroscopy, in: Springer Handbooks, Springer Science and Business Media Deutschland GmbH, 2023, pp. 3–32, https://doi.org/10.1007/978-3-031-07125-6_1.

[34] F. Zaera, New advances in the use of infrared absorption spectroscopy for the characterization of heterogeneous catalytic reactions, Chem. Soc. Rev. 43 (2014) 7624–7663, https://doi.org/10.1039/C3CS60374A.

[35] S. Campisi, M.G. Galloni, S.G. Marchetti, A. Auroux, G. Postole, A. Gervasini, Functionalized iron hydroxyapatite as eco-friendly catalyst for NH_3-SCR reaction: activity and role of iron speciation on the surface, ChemCatChem 12 (2020) 1676–1690.

[36] M. Marzo, A. Gervasini, P. Carniti, Hydrolysis of disaccharides over solid acid catalysts under green conditions, Carbohydr. Res. 347 (2012) 23–31.

[37] M.N. Catrinck, S. Campisi, P. Carniti, R.F. Teófilo, F. Bossola, A. Gervasini, Phosphate enrichment of niobium-based catalytic surfaces in relation to reactions of carbohydrate biomass conversion: the case studies of inulin hydrolysis and fructose dehydration, Catalysts 11 (2021), https://doi.org/10.3390/catal11091077.

[38] L. Delattre, F. Babonneau, ^{17}O Solution NMR characterization of the preparation of sol−gel derived SiO_2/TiO_2 and SiO_2/ZrO_2 glasses, Chem. Mater. 9 (1997) 2385–2394.

[39] J. Livage, P. Barboux, M.T. Vandenborre, C. Schmutz, F. Taulelle, Sol-gel synthesis of phosphates, J. Non-Cryst. Solids (1992) 147–148, https://doi.org/10.1016/S0022-3093(05)80586-1, 18–23.

[40] A. Bifulco, R. Avolio, S. Lehner, M.E. Errico, N.J. Clayden, R. Pauer, S. Gaan, G. Malucelli, A. Aronne, C. Imparato, In situ P-modified hybrid silica–epoxy nanocomposites via a green hydrolytic sol–gel route for flame-retardant applications, ACS Appl. Nano Mater. 6 (2023) 7422–7435, https://doi.org/10.1021/acsanm.3c00590.

[41] C. Imparato, A. Bifulco, G. Malucelli, A. Aronne, Solids containing Si-O-P bonds: is the hydrolytic sol-gel route a suitable synthesis strategy? J. Sol. Gel Sci. Technol. (2023) https://doi.org/10.1007/s10971-023-06241-4.

[42] V.G. Kessler, G.I. Spijksma, G.A. Seisenbaeva, S. Håkansson, D.H.A. Blank, H.J.M. Bouwmeester, New insight in the role of modifying ligands in the sol-gel processing of metal alkoxide precursors: a possibility to approach new classes of materials, J. Sol. Gel Sci. Technol. 40 (2006) 163–179, https://doi.org/10.1007/s10971-006-9209-6.

[43] C. Sanchez, J. Livage, M. Henry, F. Babonneau, Chemical modification of alkoxide precursors, J. Non-Cryst. Solids 100 (1988) 65–76.

[44] I. Ritacco, C. Imparato, L. Falivene, L. Cavallo, A. Magistrato, L. Caporaso, M. Farnesi Camellone, A. Aronne, Spontaneous production of ultrastable reactive oxygen species on titanium oxide surfaces modified with organic ligands, Adv. Mater. Interfaces 8 (2021) 2100629, https://doi.org/10.1002/admi.202100629.

[45] C. Imparato, M. Fantauzzi, C. Passiu, I. Rea, C. Ricca, U. Aschauer, F. Sannino, G. D'Errico, L. De Stefano, A. Rossi, A. Aronne, Unraveling the Charge State of Oxygen Vacancies in ZrO_{2-x} on the Basis of Synergistic Computational and Experimental Evidence, J. Phys. Chem. C 123 (2019) 11581–11590. https://doi.org/10.1021/acs.jpcc.9b00411.

[46] Safety Data Sheets, https://www.fishersci.it/store/msds?partNumber=10133780&countryCode=IT&language=en (accessed December 2023).

[47] R.A. Sheldon, The E factor at 30: a passion for pollution prevention, Green Chem. 25 (2023) 1704–1728, https://doi.org/10.1039/d2gc04747k.

[48] M.J. Eckelman, J.B. Zimmerman, P.T. Anastas, Toward green nano: E-factor analysis of several nanomaterial syntheses, J. Ind. Ecol. 12 (2008) 316–328, https://doi.org/10.1111/j.1530-9290.2008.00043.x.

[49] C. Gérardin, J. Reboul, M. Bonne, B. Lebeau, Ecodesign of ordered mesoporous silica materials, Chem. Soc. Rev. 42 (2013) 4217–4255, https://doi.org/10.1039/c3cs35451b.

[50] A. Maity, V. Polshettiwar, Scalable and sustainable synthesis of size-controlled monodisperse dendritic fibrous nanosilica quantified by e-factor, ACS Appl. Nano Mater. 1 (2018) 3636–3643, https://doi.org/10.1021/acsanm.8b00761.

[51] P.I. Dassie, R. Haddad, M. Lenez, A. Chaumonnot, M. Boualleg, P. Legriel, A. Styskalik, B. Haye, M. Selmane, D.P. Debecker, C. Sanchez, C. Chaneac, C. Boissiere, Coupling of solvent-free synthesis and reactive extrusion of alumina: an ecologically efficient integration for heterogenous catalyst synthesis, Green Chem. 25 (2023) 2800–2814, https://doi.org/10.1039/d2gc04714d.

[52] S. García-Granda, S.A. Khainakov, A. Espina, J.R. García, G.R. Castro, J. Rocha, L. Mafra, Revisiting the thermal decomposition of layered γ-titanium phosphate and structural elucidation of its intermediate phases, Inorg. Chem. 49 (2010) 2630–2638, https://doi.org/10.1021/ic901254j.

[53] P. Zhao, B. Boekfa, T. Nishitoba, N. Tsunoji, T. Sano, T. Yokoi, M. Ogura, M. Ehara, Theoretical study on ^{31}P NMR chemical shifts of phosphorus-modified CHA zeolites, Microporous Mesoporous Mater. 294 (2020) 109908, https://doi.org/10.1016/j.micromeso.2019.109908.
[54] C.C. Liu, G.E. Maciel, The fumed silica surface: a study by NMR, J. Am. Chem. Soc. 118 (1996) 5103–5119.
[55] J.-H. Choy, J.-B. Yoon, H. Jung, J.-H. Park, Zr K-edge XAS and ^{29}Si MAS NMR studies on hexagonal mesoporous zirconium silicate, J. Porous Mater. 11 (2004) 123–129.
[56] V. Degirmenci, Ö.F. Erdem, O. Ergun, A. Yilmaz, D. Michel, D. Uner, Synthesis and NMR characterization of titanium and zirconium oxides incorporated in SBA-15, in: Top. Catal., Springer, 2008, pp. 204–208, https://doi.org/10.1007/s11244-008-9078-z.
[57] N.J. Clayden, A. Aronne, S. Esposito, P. Pernice, Solid state NMR study of phosphosilicate gels, J. Non-Cryst. Solids 345 (2004) 601–604.
[58] C. Schmutz, P. Barboux, F. Ribot, F. Taulelle, M. Verdaguer, C. Fernandez-Lorenzo, EXAFS, Raman and ^{31}P NMR study of amorphous titanium phosphates, J. Non-Cryst. Solids 170 (1994) 250–262, https://doi.org/10.1016/0022-3093(94)90054-X.
[59] A. Aronne, M. Turco, G. Bagnasco, P. Pernice, M. Di Serio, N.J. Clayden, E. Marenna, E. Fanelli, Synthesis of high surface area phosphosilicate glasses by a modified sol−gel method, Chem. Mater. 17 (2005) 2081–2090.
[60] S. Klein, S. Thorimbert, W.F. Maier, Amorphous microporous titania–silica mixed oxides: preparation, characterization, and catalytic redox properties, J. Catal. 163 (1996) 476–488.
[61] H. Yamashita, S. Kawasaki, Y. Ichihashi, M. Harada, M. Takeuchi, M. Anpo, G. Stewart, M.A. Fox, C. Louis, M. Che, Characterization of titanium−silicon binary oxide catalysts prepared by the sol−gel method and their photocatalytic reactivity for the liquid-phase oxidation of 1-octanol, J. Phys. Chem. B 102 (1998) 5870–5875.
[62] F. Del Monte, W. Larsen, J.D. Mackenzie, Chemical interactions promoting the ZrO_2 tetragonal stabilization in ZrO_2–SiO_2 binary oxides, J. Am. Ceram. Soc. 83 (2000) 1506–1512.
[63] A. Infantes-Molina, J. Mérida-Robles, P. Maireles-Torres, E. Finocchio, G. Busca, E. Rodríguez-Castellón, J.L.G. Fierro, A. Jiménez-López, A new low-cost synthetic route to obtain zirconium containing mesoporous silica, Microporous Mesoporous Mater. 75 (2004) 23–32.
[64] K. Hadjiivanov, Identification and characterization of surface hydroxyl groups by infrared spectroscopy, Adv. Catal. 57 (2014) 99–318, https://doi.org/10.1016/B978-0-12-800127-1.00002-3.
[65] N. Stegmann, C. Ochoa-Hernández, K.-N. Truong, H. Petersen, C. Weidenthaler, W. Schmidt, The mechanism and pathway of selective partial oxidation of n-butane to maleic anhydride studied on titanium phosphate catalysts, ACS Catal. 13 (2023) 15833–15840, https://doi.org/10.1021/acscatal.3c03172.
[66] G. Busca, The surface acidity of solid oxides and its characterization by IR spectroscopic methods. An attempt at systematization, Phys. Chem. Chem. Phys. 1 (1999) 723–736, https://doi.org/10.1039/A808366E.
[67] K.D. Kim, J. Kim, W.Y. Teoh, J.-C. Kim, J. Huang, R. Ryoo, Cascade reaction engineering on zirconia-supported mesoporous MFI zeolites with tunable Lewis–Brønsted acid sites: a case of the one-pot conversion of furfural to γ-valerolactone, RSC Adv. 10 (2020) 35318–35328.
[68] R. Maderuelo-Solera, S. Richter, C.P. Jiménez-Gómez, C. García-Sancho, F. J. García-Mateos, J.M. Rosas, R. Moreno-Tost, J.A. Cecilia, P. Maireles-Torres, Porous SiO_2 nanospheres modified with ZrO_2 and their use in one-pot catalytic processes to obtain value-added chemicals from furfural, Ind. Eng. Chem. Res. 60 (2021) 18791–18805.
[69] A.T.Y. Wolek, K.E. Hicks, J.M. Notestein, Tuning acidity in silica-overcoated oxides for hydroalkoxylation, J. Catal. 426 (2023) 113–125.
[70] C.U.I. Odenbrand, J.G.M. Brandin, G. Busca, Surface acidity of silica-titania mixed oxides, J. Catal. 135 (1992) 505–517.
[71] G. Kumar, L. Ren, Y. Pang, X. Li, H. Chen, J. Gulbinski, P.J. Dauenhauer, M. Tsapatsis, O.A. Abdelrahman, Acid sites of phosphorus-modified zeosils, ACS Catal. 11 (2021) 9933–9948.
[72] V. Sanchez Escribano, G. Garbarino, E. Finocchio, G. Busca, γ-Alumina and amorphous silica–alumina: structural features, acid sites and the role of adsorbed water, Top. Catal. 60 (2017) 1554–1564, https://doi.org/10.1007/s11244-017-0838-5.
[73] G. Busca, Acidity and basicity of zeolites: a fundamental approach, Microporous Mesoporous Mater. 254 (2017) 3–16.

Supplementary material

for

Insight into titanium and zirconium phosphate-based materials for reactive surfaces

Claudio Imparato[a], Elisabetta Finocchio[b], Sebastiano Campisi[c], Michele Bigica[c], Antonella Gervasini[c,], Aurelio Bifulco[a], Roberto Avolio[d], Nigel J. Clayden[e], Maria E. Errico[d], Antonio Aronne[a,]**

[a]Dipartimento di Ingegneria Chimica, dei Materiali e della Produzione Industriale, Università degli Studi di Napoli Federico II, P.le Tecchio 80, 80125, Naples, Italy

[b]Dipartimento di Ingegneria Civile, Chimica e Ambientale, Università degli Studi di Genova, Via Opera Pia 15, 16145 Genoa, Italy

[c]Dipartimento di Chimica, Università degli Studi di Milano, Via Camillo Golgi 19, 20133, Milan, Italy

[d]Institute for Polymers, Composites and Biomaterials, National Research Council of Italy, Via Campi Flegrei 34, 80078 Pozzuoli, Naples, Italy

[e]School of Chemistry, University of East Anglia, Norwich NR4 7TJ, U.K.

* corresponding authors: antonella.gervasini@unimi.it (A.G.); antonio.aronne@unina.it (A.A.)

Section S1. Synthesis of the materials

Table S1. Molar ratios between the components of the reaction mixture in the sol-gel synthesis of the two studied samples (Me = Ti or Zr).

Sample	Me alkoxide	H_3PO_4	TEOS	Hacac	AcOH	H_2O	EtOH
TiPSi	1	0.5	8.75	1	6	35	58
ZrPSi	1	0.5	8.75	2	2	35	58

Table S2. Nominal molar and mass composition of the two studied samples, considering the oxide stoichiometry as 10 $MeO_2 \cdot 2.5\ P_2O_5 \cdot 87.5\ SiO_2$ (Me = Ti or Zr).

Sample	Me	P	Si	Me	P	Si	O
	mol%			wt.%			
TiPSi	9.8	4.9	85.3	7.5	2.4	38.3	51.8
ZrPSi	9.8	4.9	85.3	13.3	2.3	35.9	48.5

Figure S1. Photograph of a TiPSi wet gel.

Section S2. Study of reaction kinetics

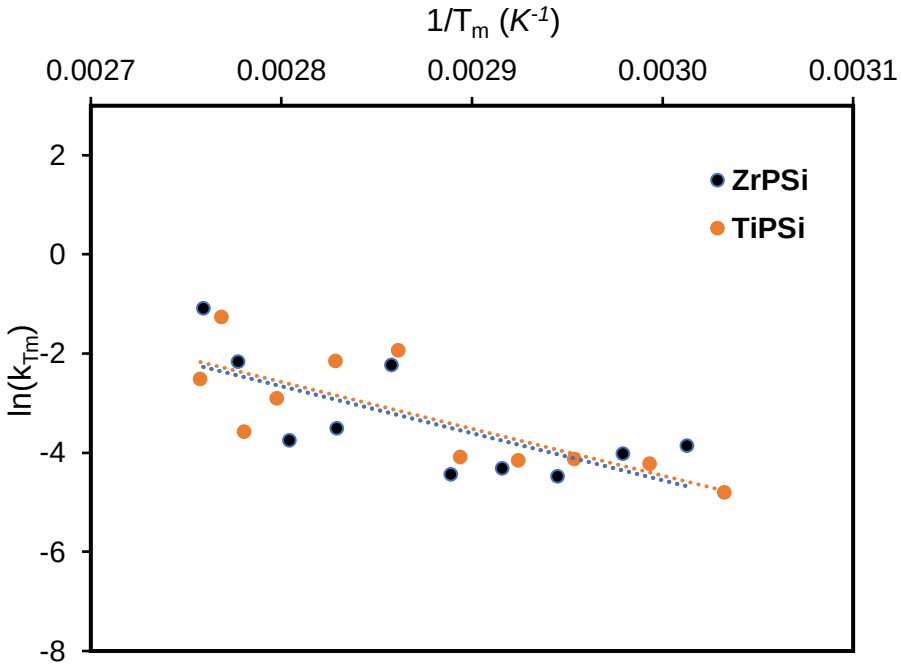

Figure S2. Arrhenius plot for sucrose hydrolysis over acid ternary oxide catalysts.

Table S3. Arrhenius coefficients for the catalytic hydrolysis of sucrose over ternary oxides. The parameters are calculated in the range of conversion from 0.5% to 40% following the temperature range from 50 to 90 °C (temperature rate: 0.12 °C min^{-1}).

Catalyst	E_a (kJ mol^{-1})	ln(A)
TiPSi	78.5 ± 21.1	23.9 ± 7.3
ZrPSi	78.8 ± 27.9	23.9 ± 9.7

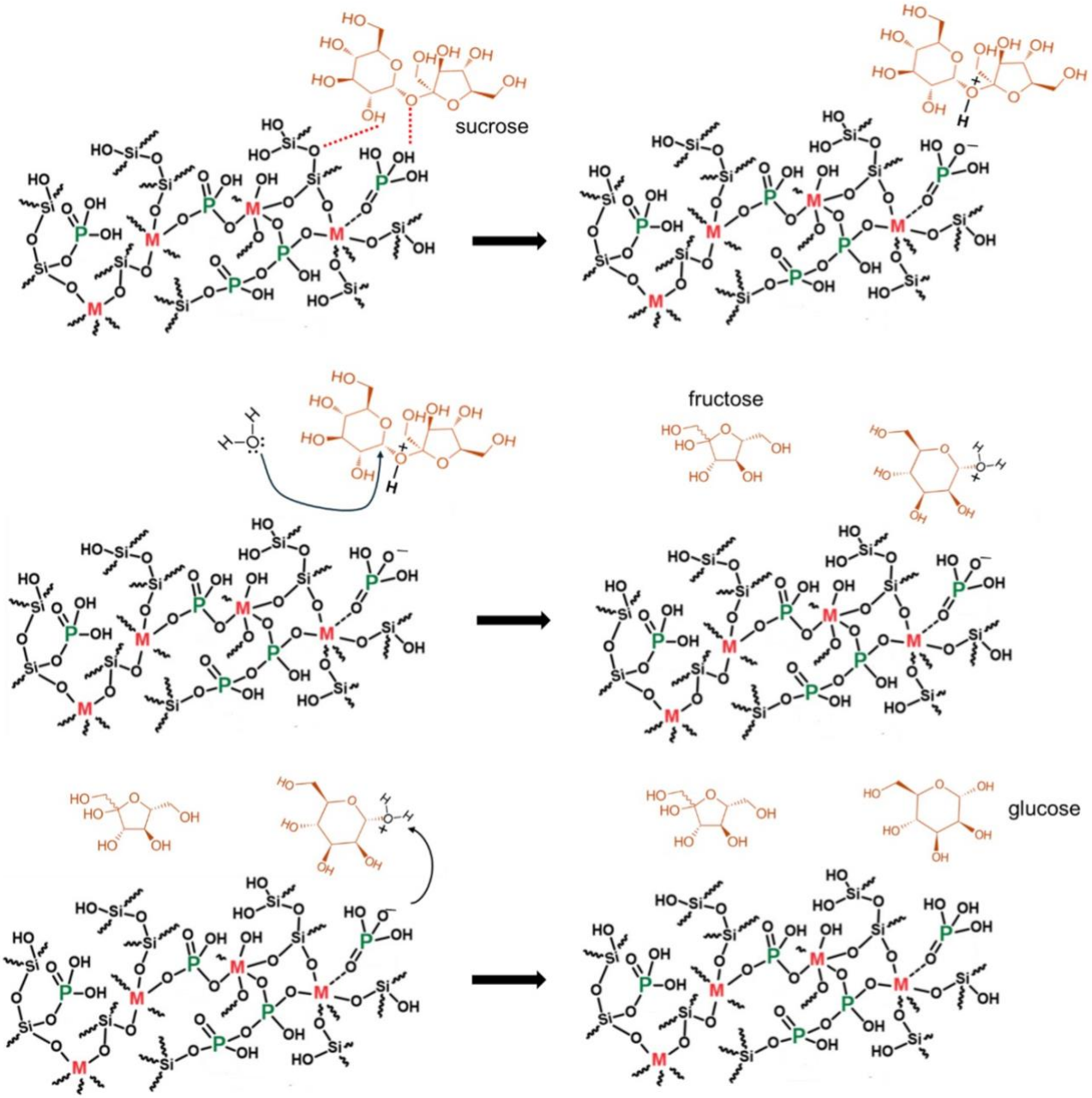

Scheme S1. Proposed mechanism for sucrose hydrolysis over acid ternary oxides involving strong Brønsted acid sites of phosphate groups.

Section S3. Evaluation of the sustainability of the synthetic route

E factors calculation. The Environmental factors, namely E factor (EF), complete E Factor (cEF) and simple E Factor (sEF), were calculated through the following equations [1,2]:

$$EF = [m_{(total)} - m_{(product)} - m_{(water)}] / m_{(product)} \quad (S1)$$

$$cEF = [m_{(total)} - m_{(product)}] / m_{(product)} \quad (S2)$$

$$sEF = [m_{(total)} - m_{(product)} - m_{(water)} - \Sigma\, m_{(solvents)}] / m_{(product)} \quad (S3)$$

The basis for the calculations is the mass composition of the selected samples, reported in each paper and included in Table S4 (Ti and P wt%). The total mass, $m_{(total)}$, is the sum of the masses of all substances used in the synthesis process: precursors, catalysts, templating/structure directing agents, auxiliaries, and solvents. The corresponding data, listed in Table S5, were obtained from the experimental sections of the relative papers. For all the studied cases, the yield of the process was considered equal to 100%. This can lead to an underestimation of the real factors in relation to the incomplete conversion of the precursors into the final product and to losses during the recovery of the material, especially for multistep procedures requiring repeated washing cycles. In some papers, the exact volumes of solvent (either organic or water) used in the washing process are not reported (see the notes in Table S5), which also causes underestimation of EF and cEF, while it does not affect sEF. No recycling of water or solvents was considered.

Among the works mentioned in Table S4, three were not included in the E factor comparison. In the paper of Kovalchuk et al. the data about the second step of the preparation are not sufficient for a reliable evaluation, while the materials studied by Uma et al. and Castro et al. were addressed to the study of Ti-P-Si glasses in proton conducting membranes; particularly, Castro et al. prepared a system with a composition very different from that of our material, which was loaded in a polymer-based hybrid membrane. The study by Paul et al. also describes a material with a composition far from ours, however it was included as a reference single-step method.

A direct comparison of functional performances between our materials and those described in the literature is not possible because they were tested in different processes. However, available data concerning important properties related to the reactivity, i.e. specific surface area, pore volume and acid sites density, were reported in Table S4.

Table S4. Resume of the methodology and operating conditions adopted for the synthesis of Ti-P-Si oxides in this work and relevant literature reports; composition and main features of selected samples. EISA: evaporation-induced self-assembly; HT: hydrothermal treatment; TMP: trimethyl phosphite; TMPO: trimethyl phosphate.

Source	**This work**	**Alfaya et al. (1998)**	**Paul et al. (2010)**	**Zhang et al. (2009)**	**Guo et al. (2022)**	**Kovalchuk et al. (2005)**	**Uma et al. (2006)**	**Castro et al. (2015)**
Method	1 step: sol-gel	2 steps: sol-gel, impregn.	1 step: EISA	2-3 steps: sol-gel, grafting	3 steps: HT, grafting, impregn.	2 steps: precipit. + HT, impregn.	1 step: sol-gel	1 step: sol impregn.
Precursors	TEOS $Ti(BuO)_4$ H_3PO_4	TEOS $Ti(BuO)_4$ H_3PO_4	TEOS $Ti(BuO)_4$ TMP	TEOS $Ti(i\text{-}PrO)_4$ H_3PO_4	TEOS $Ti(i\text{-}PrO)_4$ $POCl_3$	TEOS $Ti(BuO)_4$ $POCl_3$	TEOS $Ti(i\text{-}PrO)_4$ TMPO	TEOS $Ti(i\text{-}PrO)_4$ TMPO
Additives	Hacac acetic acid	HNO_3	HCl acetic acid F127	HCl P123	HCl P123	NaOH MTMAB	HCl	Hacac HCl P123
Solvents	EtOH	EtOH	EtOH	toluene EtOH water	toluene, water	i-PrOH toluene	EtOH DMF	PrOH
Heat treatment	500 °C/1 h	500 °C/ 120 h	400 °C/6 h	500 °C/6 h	550 °C/6 h	180 °C/2 h 540 °C/4 h	540 °C/4 h	540 °C/4 h
Ti (wt%)	7.5	10.8 [a]	25	6.7 [b]	5.6 [c]	6.5	3.6 [d]	14
P (wt%)	2.4	2.2 [a]	10	6.2 [b]	3.7 [c]	7.9	5.6 [d]	18
SSA [e] (m^2/g)	395	465 [a]	379	462 [b]	594 [c]	510	402 [d]	301
Pore vol. (cm^3/g)	0.19	0.41 [a]	N.A.	0.52 [b]	0.82 [c]	0.22	0.24 [d]	0.28
Acid sites [f] (µmol/g)	744	N.A.	N.A.	N.A.	123 [c]	480-1130	N.A.	N.A.
Ref.	-	[3]	[4]	[5]	[6]	[7]	[8]	[9]

[a] sample STP2 (intermediate Ti and P content)

[b] sample SBA-15-TiP (2-step synthesis with one grafting cycle)

[c] sample P-1Ti/SBA-15 (one TiO_2 grafting cycle)

[d] sample T1 (lowest P content)

[e] Specific Surface Area measured by BET method

[f] density of acid sites determined by NH_3 TPD measurements.

Table S5. Values of E factor (including all used chemicals except water), complete E Factor (cEF, including all used chemicals and assuming no recycling), and simple E Factor (sEF, excluding water and solvents) for the synthesis of Ti-P-Si oxide material in this work and relevant literature reports. Total masses (kg) of all the chemicals used in the synthesis of 1 kg of product, considering the same samples whose features are listed in Table S3 (TMP: trimethyl phosphite; TMPO: trimethyl phosphate).

Source	**This work**	**Alfaya et al. (1998)** [a]	**Paul et al. (2010)**	**Zhang et al. (2009)** [b]	**Guo et al. (2022)** [c]
cE factor	**9.4**	**18.4** [d]	**20.2**	**180.4** [e]	**143.1** [d]
E factor	**8.3**	**13.8** [d]	**19.3**	**67.3** [e]	**22.9** [d]
sE factor	**3.6**	**2.6**	**5.8**	**7.0**	**8.6**
Compound	Mass (kg)				
TEOS	3.13	2.67	1.19	2.59	2.85
$Ti(BuO)_4$	0.587	0.770	1.94	-	-
$Ti(i\text{-}PrO)_4$	-	-	-	0.725	0.796
H_3PO_4	0.085	0.083	-	-	4.65
TMP	-	-	0.354	-	-
$POCl_3$	-	-	-	1.17	-
Hacac	0.173	-	-	-	-
P123/F127	-	-	1.37	1.22	1.26
Acetic acid	0.620	-	1.37	-	-
HCl	-	-	0.529	2.25	0.056
HNO_3	-	0.068	-	-	-
EtOH	4.67	11.20	13.54	0.790	-
Toluene	-	-	-	59.6	14.3
Water	1.09	4.60	0.930	113.1	120.2
Total mass	10.35	19.39	21.23	181.43	144.12
Ref.	-	[3]	[4]	[5]	[6]

[a] sample STP2 (intermediate Ti and P content)

[b] sample SBA-15-TiP (2-step synthesis with one grafting cycle)

[c] sample P-1Ti/SBA-15 (one TiO_2 grafting cycle)

[d] solvent used in product washing not considered (unavailable data)

[e] solvent used in product washing underestimated (incomplete data).

References

1 R. A. Sheldon, The E factor at 30: a passion for pollution prevention *Green Chem.*, 2023, **25**, 1704–1728.

2 M. Palencia, A. García-Quintero and V. J. Palencia Luna, Metrics for the Sustainability Analysis of Nano-synthesis in the Green Chemistry Approach, in *Handb. Green Sustain. Nanotechnol.*, 2023, 1911–1935.

3 A. A. S. Alfaya, Y. Gushikem and S. C. De Castro, Highly Dispersed Phosphate Supported in a Binary Silica-Titania Matrix: Preparation and Characterization, *Chem. Mater.*, 1998, **10**, 909–913.

4 M. Paul, N. Pal, M. Ali and A. Bhaumik, New mesoporous silicotitaniumphosphate and its application in acid catalysis and adsorption of As(III/V), Cd(II) and Hg(II), *J. Mol. Catal. A Chem.*, 2010, **330**, 49–55.

5 J. Zhang, Z. Ma, J. Jiao, H. Yin, W. Yan, E. W. Hagaman, J. Yu and S. Dai, Layer-by-layer grafting of titanium phosphate onto mesoporous silica SBA-15 surfaces: synthesis, characterization, and applications, *Langmuir*, 2009, **25**, 12541–12549.

6 W. Guo, E. J. M. Hensen, W. Qi, H. J. Heeres and J. Yue, Titanium Phosphate Grafted on Mesoporous SBA-15 Silica as a Solid Acid Catalyst for the Synthesis of 5-Hydroxymethylfurfural from Glucose, *ACS Sustain. Chem. Eng.*, 2022, **10**, 10157–10168.

7 T. V. Kovalchuk, H. Sfihi, A. S. Korchev, A. S. Kovalenko, V. G. Il'in, V. N. Zaitsev and J. Fraissard, Synthesis, structure, and acidic properties of MCM-41 functionalized with phosphate and titanium phosphate groups, *J. Phys. Chem. B*, 2005, **109**, 13948–13956.

8 T. Uma, S. Izuhara and M. Nogami, Structural and proton conductivity study of P_2O_5-TiO_2-SiO_2 glasses, *J. Eur. Ceram. Soc.*, 2006, **26**, 2365–2372.

9 Y. Castro, J. Mosa, M. Aparicio, L. A. Pérez-Carrillo, S. Vílchez, J. Esquena and A. Durán, Solegel hybrid membranes loaded with meso/macroporous SiO_2, TiO_2-P_2O_5 and SiO_2-TiO_2-P_2O_5 materials with high proton conductivity, *Mater. Chem. Phys.*, 2015, **149**, 686–694.

Section S4. Characterization of the materials

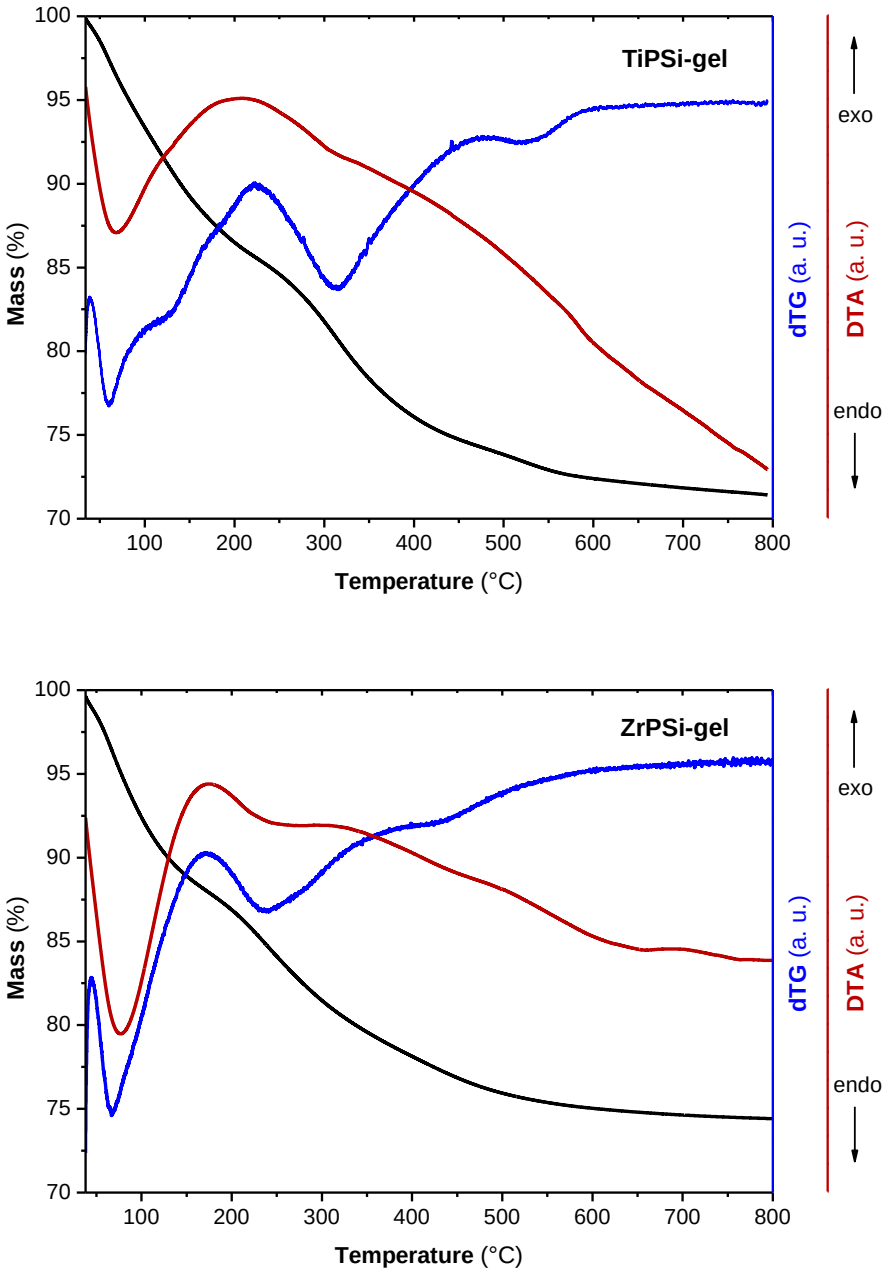

Figure S3. TGA, dTG and DTA curves of TiPSi (top) and ZrPSi (bottom) dried gels.

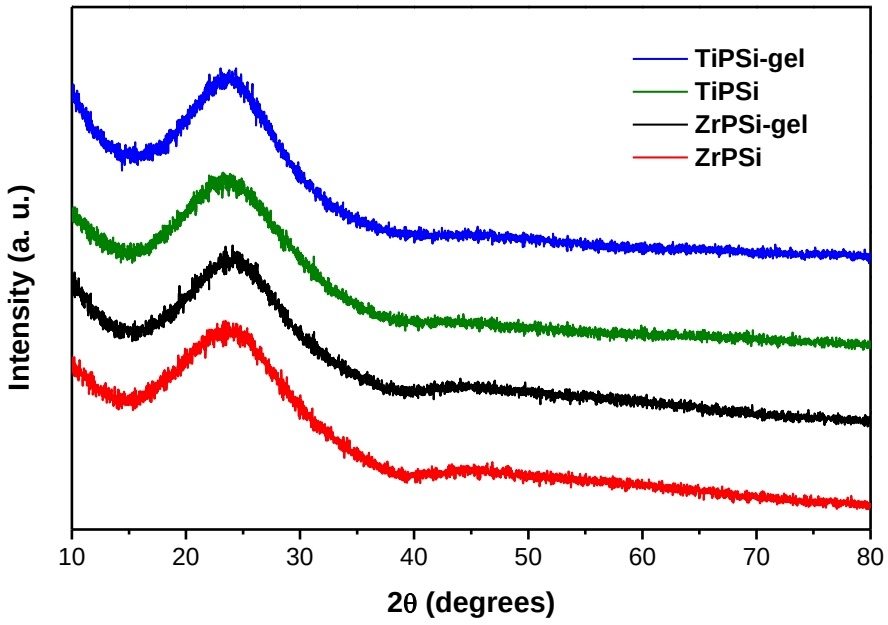

Figure S4. XRD patterns of the dried gels and calcined powder samples.

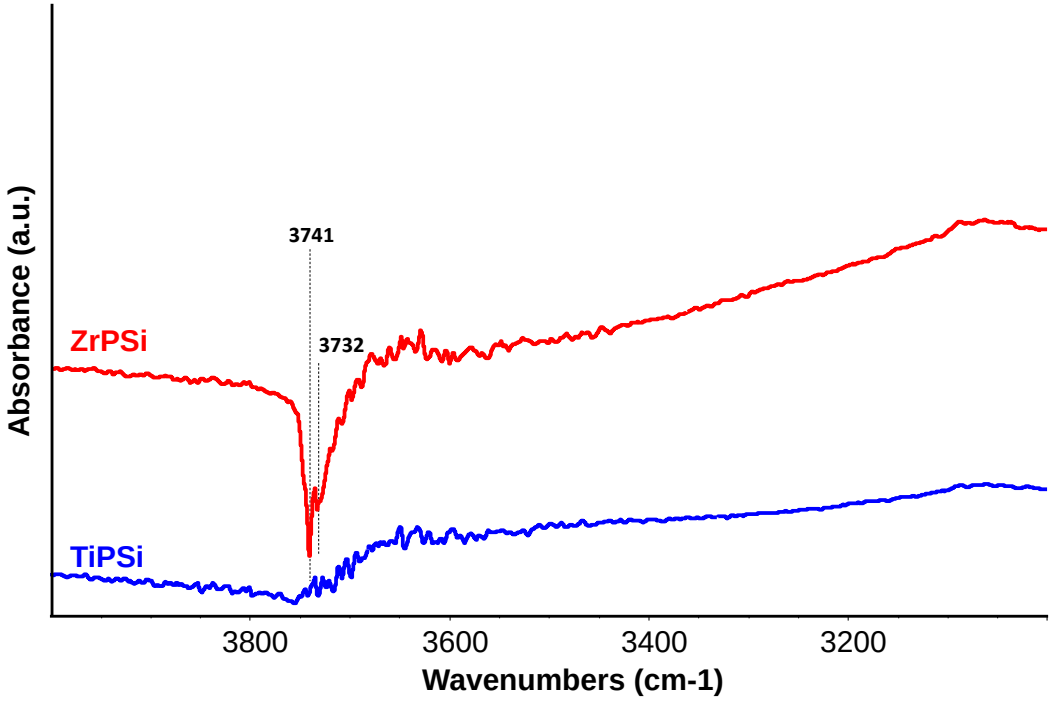

Figure S5. FTIR subtraction spectra of catalysts surface after PY adsorption and outgassing at room temperature. OH stretching region.

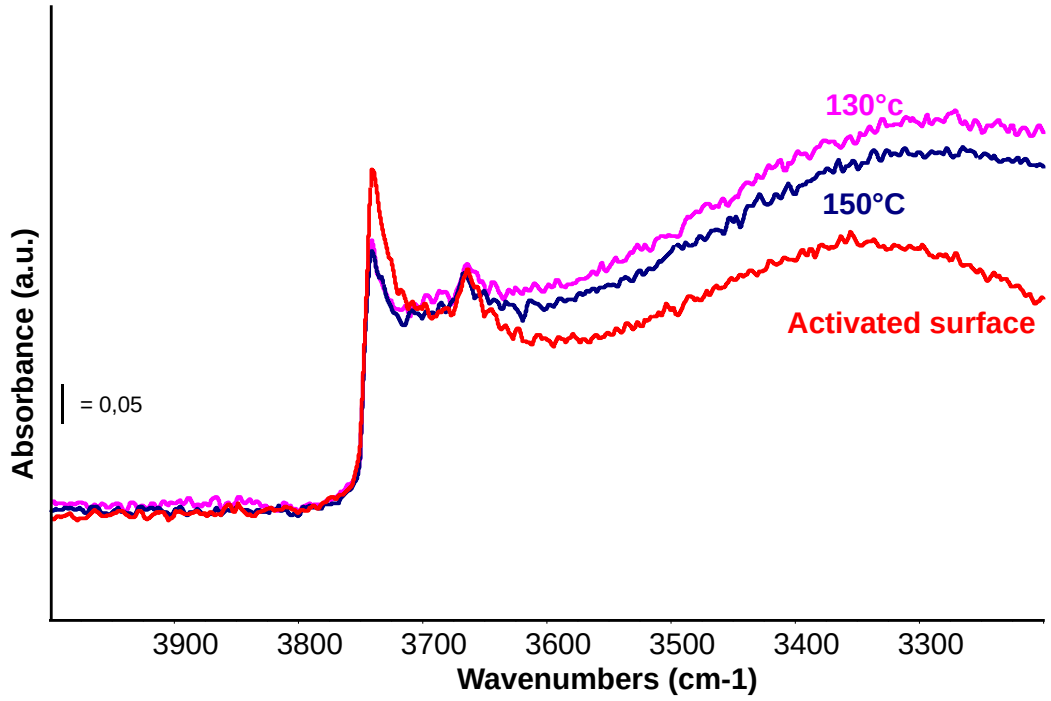

Figure S6. FTIR spectra of catalysts surface after PY adsorption and outgassing at increasing temperature. OH stretching region.

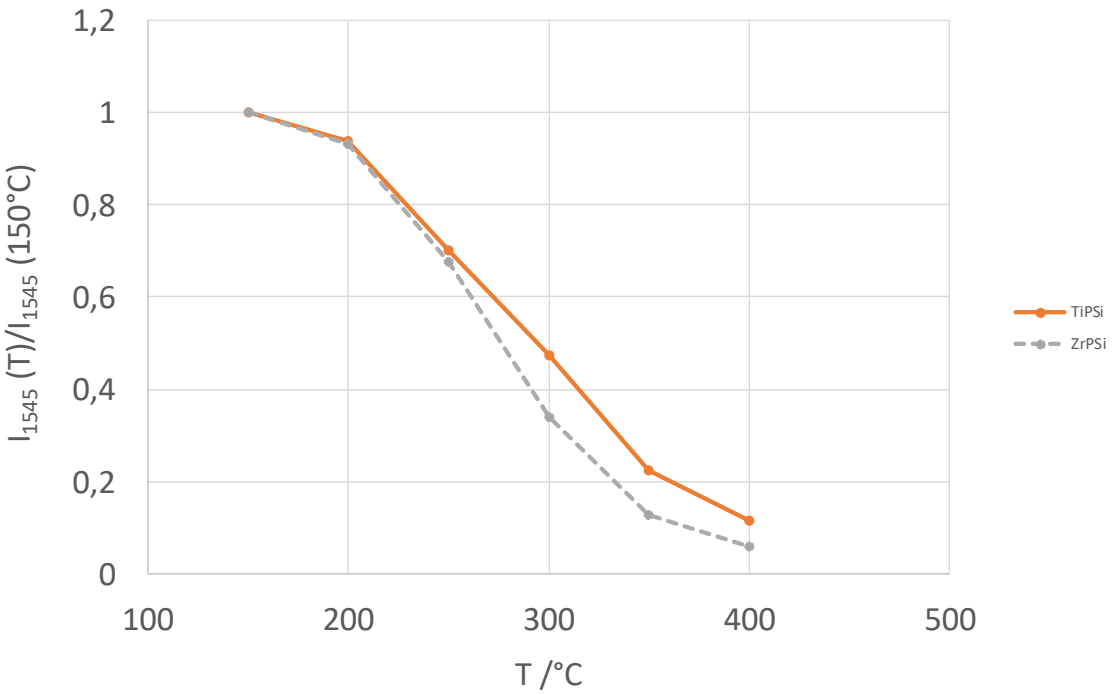

Figure S7. PYH^+ band intensity ratio vs. temperature. The band area has been normalized to the initial value (band area @423 K).